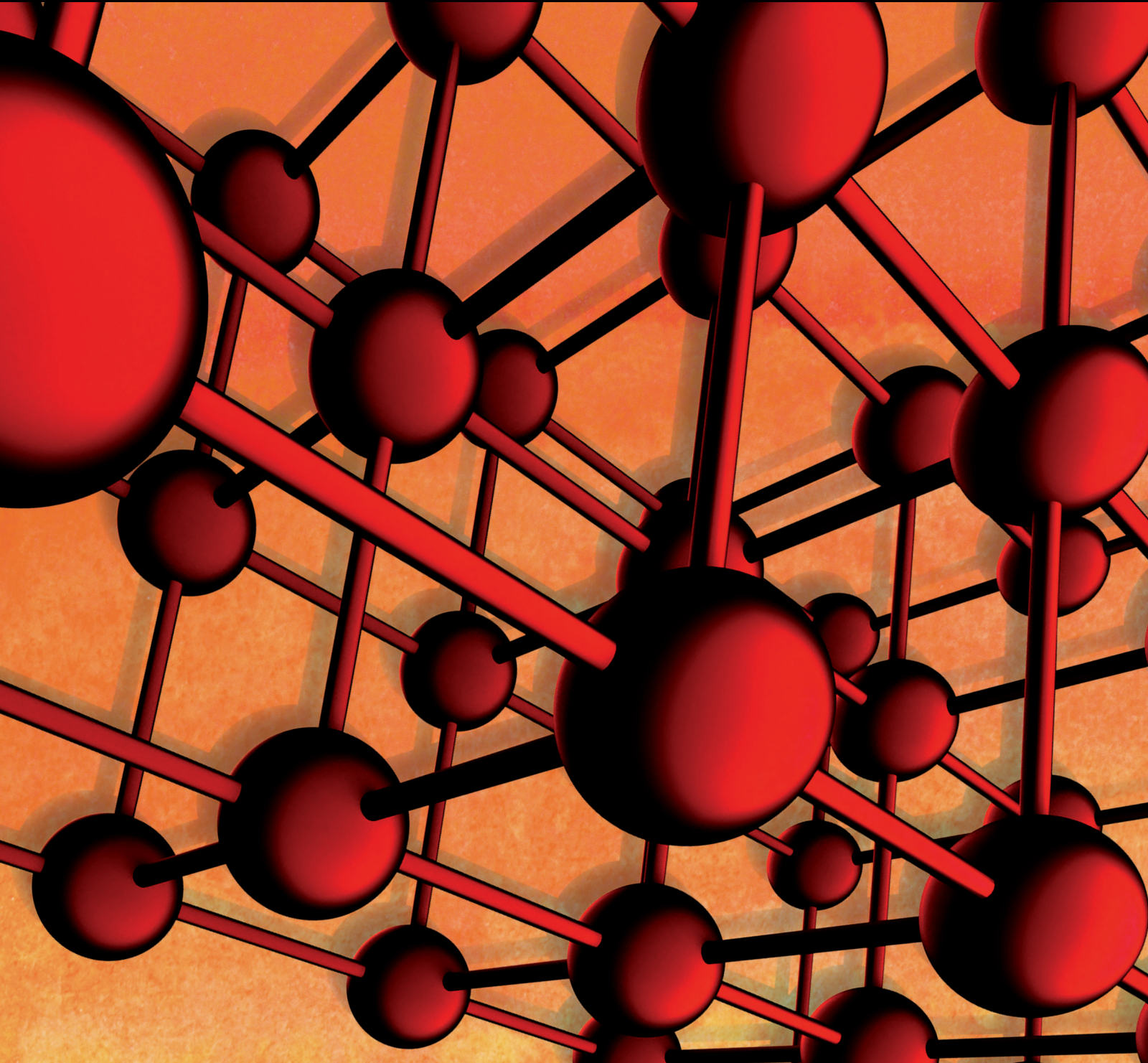


Advances in Materials Science and Engineering

High-Entropy Alloys

Guest Editors: Yong Zhang, Jien-Wei Yeh, Jian F. Sun, Jun P. Lin, and Ke-Fu Yao





High-Entropy Alloys

Advances in Materials Science and Engineering

High-Entropy Alloys

Guest Editors: Yong Zhang, Jien-Wei Yeh, Jian F. Sun,
Jun P. Lin, and Ke-Fu Yao



Copyright © 2015 Hindawi Publishing Corporation. All rights reserved.

This is a special issue published in “Advances in Materials Science and Engineering.” All articles are open access articles distributed under the Creative Commons Attribution License, which permits unrestricted use, distribution, and reproduction in any medium, provided the original work is properly cited.

Editorial Board

- Dimitrios G. Aggelis, Belgium
Jarir Aktaa, Germany
K. G. Anthymidis, Greece
Amit Bandyopadhyay, USA
Arun Bansil, USA
Massimiliano Barletta, Italy
Jozef Bednarcik, Germany
Avi Bendavid, Australia
Jamal Berakdar, Germany
Giovanni Berselli, Italy
Alessandra Bianco, Italy
Susmita Bose, USA
Heinz-Günter Brokmeier, Germany
Steve Bull, UK
Peter Chang, Canada
Daolun Chen, Canada
Gabriel Cuello, France
Narendra B. Dahotre, USA
João P. Davim, Portugal
Francesco Delogu, Italy
Seshu B. Desu, USA
Yong Ding, USA
Aziz Dinia, France
Kaveh Edalati, Japan
Gilbert Fantozzi, France
Massimo Fresta, Italy
E. Freysz, France
Sergi Gallego, Spain
Santiago Garcia-Granda, Spain
Filippo Giannazzo, Italy
Salvatore Grasso, UK
Daniel Guay, Canada
Hiroki Habazaki, Japan
Joke Hadermann, Belgium
Satoshi Horikoshi, Japan
Rui Huang, USA
Jacques Huot, Canada
Michele Iafisco, Italy
- Richard W. Jones, UK
Maarit Karppinen, Finland
Katsuyuki Kida, Japan
Jae-Ho Kim, Korea
Akihiko Kimura, Japan
Takayuki Kitamura, Japan
Hongchao Kou, China
Prashant Kumta, USA
Luciano Lamberti, Italy
Heinrich Lang, Germany
Bradley Layton, USA
Pavel Lejcek, Czech Republic
Cristina Leonelli, Italy
Markku Leskela, Finland
Ying Li, USA
Ying Liu, USA
Yunqi Liu, China
Wei Liu, France
Jun Liu, China
Meilin Liu, Georgia
Fernando Lusquiños, Spain
Peter Majewski, Australia
Philippe Miele, France
Hossein Moayedi, Malaysia
Paul Munroe, Australia
Rufino M. Navarro, Spain
Luigi Nicolais, Italy
Hiroshi Noguchi, Japan
Chérif Nouar, France
José L. Ocaña, Spain
Tsutomu Ohzuku, Japan
Olanrewaju Ojo, Canada
Xiaoqing Pan, USA
Anna Paradowska, Australia
Bart Partoens, Belgium
Gianluca Percoco, Italy
Jean-Francois Pierson, France
Simon C. Potter, Canada
- Manijeh Razeghi, USA
Anna Richelli, Italy
Antonio Riveiro, Spain
Pascal Roussel, France
Timo Sajavaara, Finland
Antti Salminen, Finland
Fawzy H. Samuel, Canada
Carlo Santulli, Italy
Franz-Josef Schmitt, Germany
Jainagesh A. Sekhar, USA
Fridon Shubitidze, USA
Charles C. Sorrell, Australia
Costas M. Soukoulis, USA
Sam-Shajing Sun, USA
Kohji Tashiro, Japan
Philippe Thomas, France
Somchai Thongtem, Thailand
Achim Trampert, Germany
Filip Tuomisto, Finland
Stuart Turner, Belgium
Krystyn Van Vliet, USA
Rui Vilar, Portugal
Holger von Wenckstern, Germany
Rong Wang, USA
Qiang Wang, China
Rui Wang, China
Lu Wei, China
Jörg Wiezorek, USA
Wei Wu, USA
Hemmige S. Yathirajan, India
Wenbin Yi, China
Belal F. Yousif, Australia
Ming-Xing Zhang, Australia
Li Zhang, China
Jinghuai Zhang, China
Wei Zhou, China

Contents

High-Entropy Alloys, Yong Zhang, Jien-Wei Yeh, Jian F. Sun, Jun P. Lin, and Ke-Fu Yao
Volume 2015, Article ID 781303, 1 pages

An Atomic Study of Substructures Formed by Shear Transformation in Cast γ -TiAl, Hanlei Zhang, Hongchao Kou, Xiaolei Li, Bin Tang, and Jinshan Li
Volume 2015, Article ID 675963, 6 pages

A Study of Thin Film Resistors Prepared Using Ni-Cr-Si-Al-Ta High Entropy Alloy, Ruei-Cheng Lin, Tai-Kuang Lee, Der-Ho Wu, and Ying-Chieh Lee
Volume 2015, Article ID 847191, 7 pages

Fabrication of Fe-6.5wt%Si Ribbons by Melt Spinning Method on Large Scale, Y. F. Liang, S. Wang, H. Li, Y. M. Jiang, F. Ye, and J. P. Lin
Volume 2015, Article ID 296197, 5 pages

The Microstructures and Electrical Resistivity of (Al, Cr, Ti)FeCoNiO_x High-Entropy Alloy Oxide Thin Films, Chun-Huei Tsau, Zhang-Yan Hwang, and Swe-Kai Chen
Volume 2015, Article ID 353140, 6 pages

Torsion Dependence of Domain Transition and MI Effect of Melt-Extracted Co_{68.15}Fe_{4.35}Si_{12.25}B_{13.25}Nb₁Cu₁ Microwires, Dawei Xing, Dongming Chen, Fang Liu, Jingshun Liu, Hongxian Shen, Zhiliang Ning, Fuyang Cao, and Jianfei Sun
Volume 2015, Article ID 958341, 6 pages

The Effect of Stoichiometry on Hydrogen Embrittlement of Ordered Ni₃Fe Intermetallics, Y. X. Chen, Tao Chen, and Haiyan Qian
Volume 2015, Article ID 504207, 6 pages

Editorial

High-Entropy Alloys

Yong Zhang,¹ Jien-Wei Yeh,² Jian F. Sun,³ Jun P. Lin,¹ and Ke-Fu Yao⁴

¹Beijing University of Science and Technology, Beijing 100083, China

²National Tsing Hua University, Hsinchu 30013, Taiwan

³Harbin Institute of Technology, Harbin 150001, China

⁴Tsinghua University, Beijing 100084, China

Correspondence should be addressed to Yong Zhang; drzhangy@ustb.edu.cn

Received 18 February 2015; Accepted 18 February 2015

Copyright © 2015 Yong Zhang et al. This is an open access article distributed under the Creative Commons Attribution License, which permits unrestricted use, distribution, and reproduction in any medium, provided the original work is properly cited.

High-entropy alloys are usually defined as metallic materials with high entropy of mixing at their disordered state. They tend to form high-entropy disordered solid solutions and amorphous phases and get simpler microstructure. High-entropy alloys can include disordered solid solution alloys and high-entropy metallic glasses. In addition, high-entropy ceramics based on the same “high entropy” concept can include carbides, nitrides, borides, and oxides. Recent advances in high-entropy alloys and ceramics have brought new conceptions to develop advanced materials, which may potentially overcome the challenges in increasing the property limits for the advanced energy and environment friendly materials. Knowledge and understanding of these high-entropy alloys and ceramics have led to the usage of novel tools for more detailed study such as serration and crackling noise detection, high energy X-rays synchrotron, neutron diffraction, focus ion beam (FIB), 3-dimensional atomic probe tomography (3D APT), density functional theory modeling (DFT), CALPHAD, and ab initio molecular dynamics (AIMD) modeling.

In this special issue, investigators contribute original research articles as well as review articles that will stimulate the continuing efforts to understand the structure, phase formation rules, thermodynamics, kinetics, processing, and properties underlying the development strategies and the evaluation of outcomes. We are particularly interested in articles describing the new technologies applied for fabricating the materials and characterizing the structural change in the micro- and nanoscale by in situ observations.

The following areas are covered in this special issue: recent developments in high-entropy alloys, ceramics, and amorphous alloys; advances in mechanical and physical behaviors of high-entropy alloys; latest technologies for fabricating and characterizing high-entropy alloys; and serration behaviors and crackling noise of advanced materials.

*Yong Zhang
Jien-Wei Yeh
Jian F. Sun
Jun P. Lin
Ke-Fu Yao*

Research Article

An Atomic Study of Substructures Formed by Shear Transformation in Cast γ -TiAl

Hanlei Zhang, Hongchao Kou, Xiaolei Li, Bin Tang, and Jinshan Li

State Key Laboratory of Solidification Processing, Northwestern Polytechnical University, Xi'an 710072, China

Correspondence should be addressed to Hanlei Zhang; zhlnwpu@126.com

Received 16 October 2014; Accepted 4 December 2014

Academic Editor: Haiming Lu

Copyright © 2015 Hanlei Zhang et al. This is an open access article distributed under the Creative Commons Attribution License, which permits unrestricted use, distribution, and reproduction in any medium, provided the original work is properly cited.

Substructures and microsegregation of γ/γ laths are analyzed with HRTEM and HAADF-STEM. Results show that the substructures are generated during evolution of shear transformation on the $(11\bar{1})$ plane of γ lath. At the beginning, shear transformation evolves in a single γ lath, and a superstructure intrinsic stacking fault (SISF) forms in the γ lath. After the formation of the SISF, the shear transformation may evolve in two different ways. If the shear transformation evolves into neighboring γ laths, the SISF also penetrates into neighboring γ laths and a ribbon of SISFs forms. If shear transformation continues to evolve in the original lath, complex substructures begin to form in the original. If shear transformation in the original lath is homogeneous and complete, secondary twin forms which may further grow into twin intersection. Incomplete shear transformation could not form secondary twins but generates a high concentration of planar faults on the $(11\bar{1})$ plane. These planar faults may further penetrate the γ/γ lath interface, grow into adjacent laths, and form a ribbon of planar faults.

1. Introduction

γ -TiAl is an important low density, high strength structural alloy for application at high temperature (up to 900°C) [1, 2], which draws much attention in the field of aeronautics, astronautics, and automobiles [3, 4]. The most important microstructure of γ -TiAl is full lamellar structure, which consists of α_2 and γ laths. Fine, equiaxed full lamellar microstructure can serve excellent overall mechanical property at high temperature. The mechanical property of γ lath is heavily dependent on its substructures, and the most common substructures in the γ lath are superstructure intrinsic stacking fault (SISF), antiphase boundary (APB), and secondary twin [5]. The formation of the SISF and the secondary twin are both on the $(11\bar{1})$ plane, and it is explained by three different theories. Study [6] reveals that SISF and secondary twin form during shear transformation on the $(11\bar{1})$ plane. In a different theory, the SISF and the secondary twin may also be generated by movement of dislocations on the $(11\bar{1})$ plane [7]. Last but not least, SISF and secondary twin could form by subinterfaces. Considering all these 3 relative theories, the formation of SISF and the secondary

twin is a complex process. The complex microstructure of SISF and secondary twin should be characterized and compared, so their formation could be further explored; the growth mechanism of them can thus be studied, and an overall growth mechanism could be proposed.

In the current work, structure and segregation of SISF and secondary twin are analyzed with high resolution transmission electron microscopy (HRTEM) and high-angle annular dark-field scanning transmission electron microscopy (HAADF-STEM). Afterwards, the formation mechanism of SISF and secondary twin is proposed. With these works, the subsequent substructures of SISF that are twin intersection and a high concentration of planar faults are explored. The formation mechanisms of twin intersection and planar faults are thus discussed.

2. Experimental

Chemical composition of the alloy in this work is Ti-48Al-2Cr-2Nb (at%). The ingot was prepared by vacuum arc melting, and then the sample was prepared with investment pattern precision casting. Afterwards, the sample was

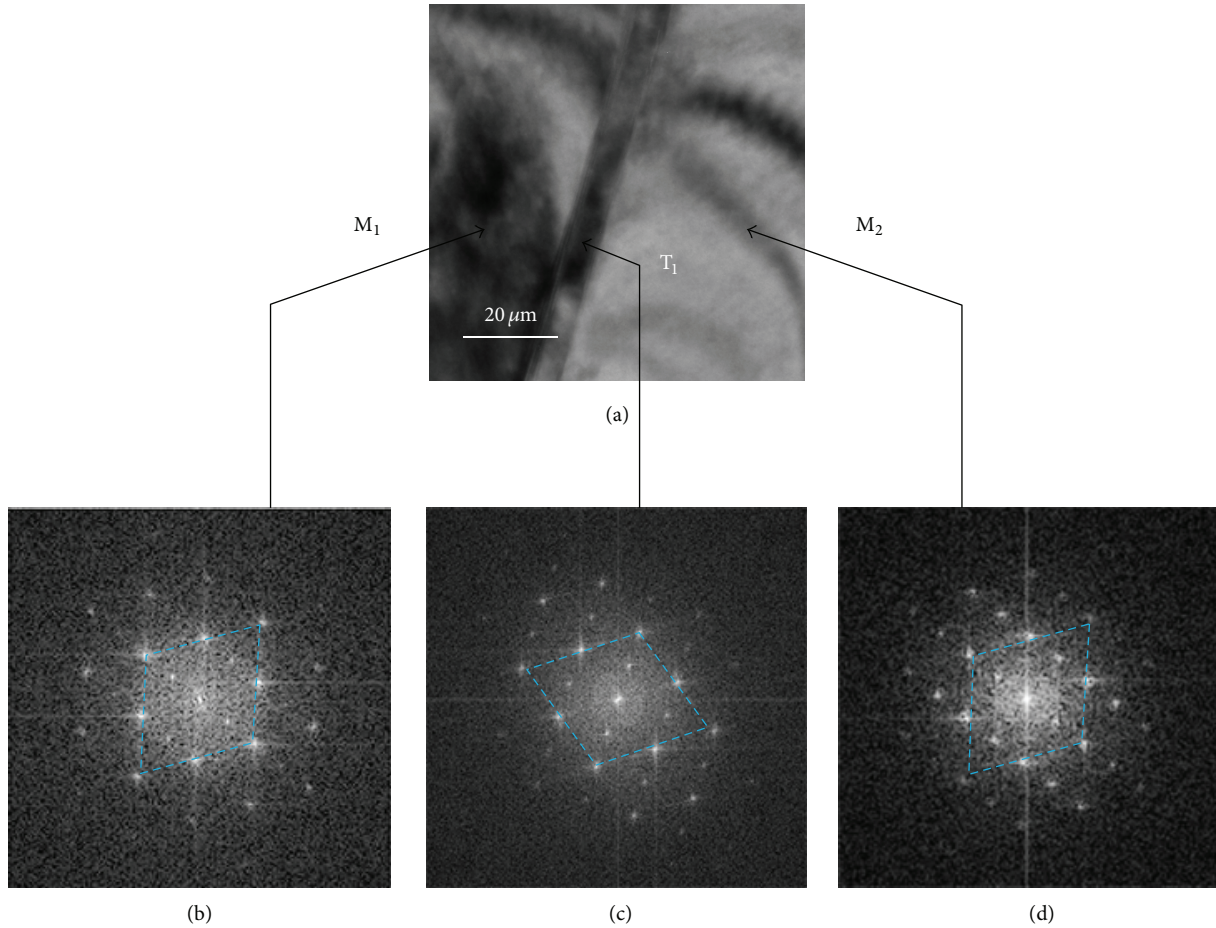


FIGURE 1: (a) A TEM graph of continuous γ laths. (b) A HAADF-STEM graph of the same region. (c) A schematic illustration of this region.

annealed in the atmosphere of argon gas at 1380°C for 1 h, followed by furnace cooling. Oxygen concentration of the sample is 200~300 ppm. Microstructure analysis, HRTEM, and HAADF-STEM were conducted with an FEI Tecnai G2 F30 transmission electron microscopy (TEM).

3. Results and Discussion

Figure 1(a) shows the TEM graph of three continuous γ laths, marked as M_1 , T_1 , and M_2 . The γ laths are continuous γ laths in the lateral direction, and no α_2 lath forms between the γ laths. The interfaces between the γ laths are γ/γ interfaces. The continuous γ laths form because, in γ -TiAl alloy, the fraction of γ lath (90 vol%) is much higher than α_2 lath. To have better understanding of the crystallographic relationship between the γ laths, fast Fourier transform (FFT) patterns of the three laths are obtained, shown in Figures 1(b), 1(c), and 1(d). Because of the symmetry in Figures 1(b), 1(c), and 1(d), it can be determined that M_1 , T_1 , and M_2 are true twins. The twinning plane is (111) plane.

Figure 2(a) shows a local HRTEM graph of the three γ laths shown in Figure 1(a). Figure 2(b) shows a HAADF-STEM graph of the same region. Figure 2(c) is a schematic illustration of the same region. When the γ laths grow in

the lateral direction, the stack sequence may change (from ABC to ACB), so twinning occurs. Twinning is an important mechanism for lateral growth. For the three twin laths, a SISF forms on the (11 $\bar{1}$) plane of T_1 . Driving force of the SISF is internal stress generated by phase transformation $\alpha \rightarrow \gamma$ [8]. On the T_1/M_2 interface, lattice distortion can be observed. On the M_1/T_1 interface there is almost no SISF, and this interface is almost a perfect twin interface. Figure 2(b) is a HAADF-STEM graph, so it manifests segregation of Ti and Al in the three laths. In Figure 2(b), the red region represents high Ti/Al ratio while the green region represents low Ti/Al ratio. As can be seen, in most parts of the γ lath, it is homogeneously green so the Ti/Al ratio is stable. Ti atoms segregate on the SISF and the T_1/M_2 interface, where the Ti/Al ratio is much higher than that inside the γ lath. On the M_1/T_1 interface, there is no clear segregation and the Ti/Al ratio is almost the same as that inside the γ lath. Considering the SISF and distortion (Figure 2(a)), it seems like that the Ti atoms tend to segregate where the lattice structure is changed.

Figure 2 characterized and discussed the structure and segregation of SISF. The formation of SISF is via propagation of $1/6[112]$ Shockley partials [9, 10]. The Shockley partial moves on the (11 $\bar{1}$) plane and causes shear transformation on the plane. Because of the shear transformation, SISF

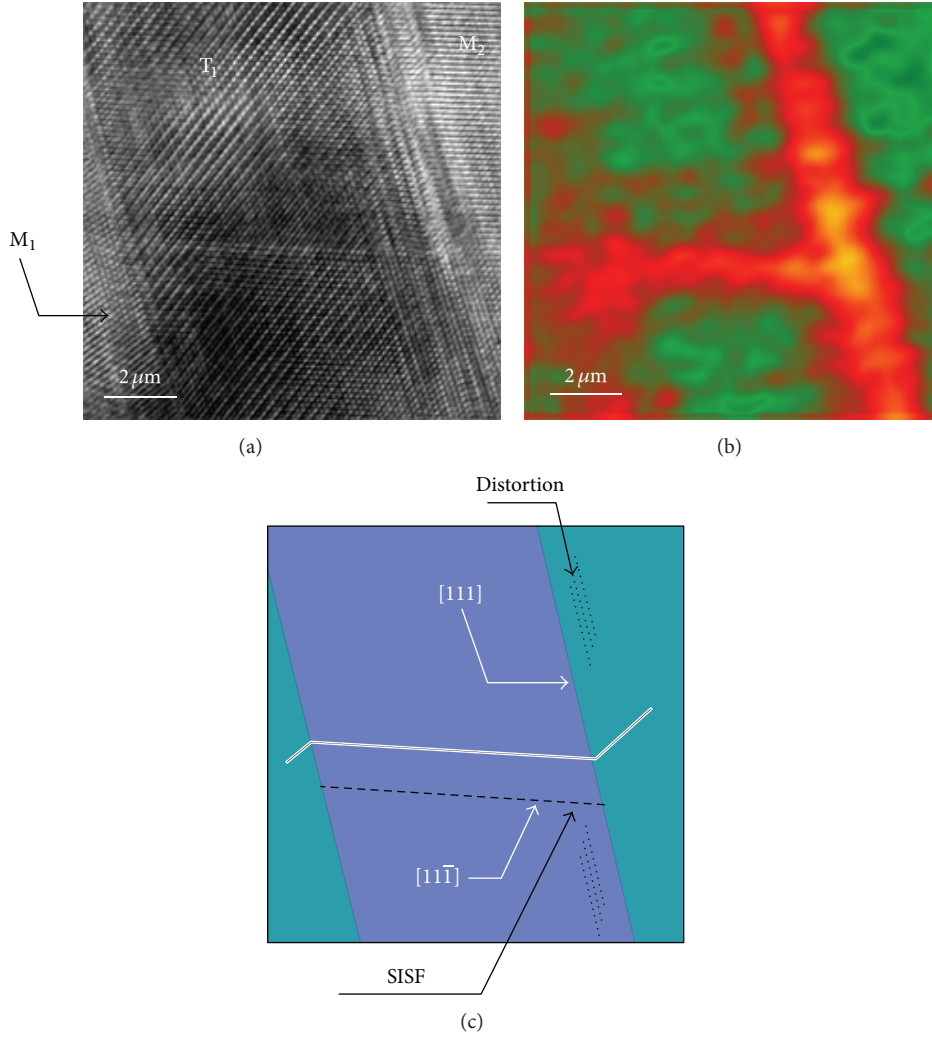
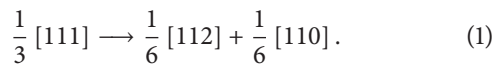


FIGURE 2: (a) A local HRTEM graph of the continuous γ laths. (b) A HAADF-STEM graph of the same region. (c) A schematic illustration of this region.

forms. Movement of 1 Shockley partial can form 1 SISF. Appel proposed that the $1/6[112]$ Shockley partials can propagate by decomposition of $1/3[111]$ dislocations [11]:



The reaction takes place on the γ/γ lath interface, where $1/3[111]$ partials are consumed and $1/6[112]$ and $1/6[110]$ partials propagate. In the cast alloy there may not be much $1/3[111]$ partials on the γ/γ lath interface [6], so $-1/3[111]$ partials may form to generate $1/3[111]$ partials. These $-1/3[111]$ partials segregate on the γ/γ lath interface, so there may be lattice distortion, as shown in Figure 2(a). After the reaction, $1/6[112]$ can travel across the γ lath, from one γ/γ interface to another. During its traveling, shear transformation may be caused on the $(11\bar{1})$ plane, and thus SISF may form. The $1/6[110]$ partials, however, could stay only at the nucleation region, so it may segregate and cause lattice distortion. In short, the $-1/3[111]$ and $1/6[110]$ partials

segregate on the nucleation region, and the $1/6[112]$ partials segregate on the other side of the γ lath. The segregation of Ti on the γ/γ lath interface and the SISF may be caused by movement of dislocations. Movement of $1/6[112]$ partials and $1/6[110]$ partials equals insert of (112) or (110) planes [12]. Considering that the (112) and (110) planes are made of one type of atoms, this dislocation movement may increase the Ti concentration on the slide plane, as shown in Figure 2(b). On the M_1/T_1 interface, no dislocation movement takes place, so the chemical composition remains unchanged. A schematic illustration of the reaction and movement of dislocations is shown in Figure 3.

The SISFs formed on the $(11\bar{1})$ plane may later penetrate into adjacent γ lath and engender SISFs in the adjacent lath, so a continuous ribbon of planar faults may exist and penetrate a few γ/γ lath interfaces, as shown in Figure 4(a). The ribbon is made of many planar faults, so it is accompanied with shear transformation on the $(11\bar{1})$ plane when it penetrates the γ laths and γ/γ lath interfaces. This shear transformation is

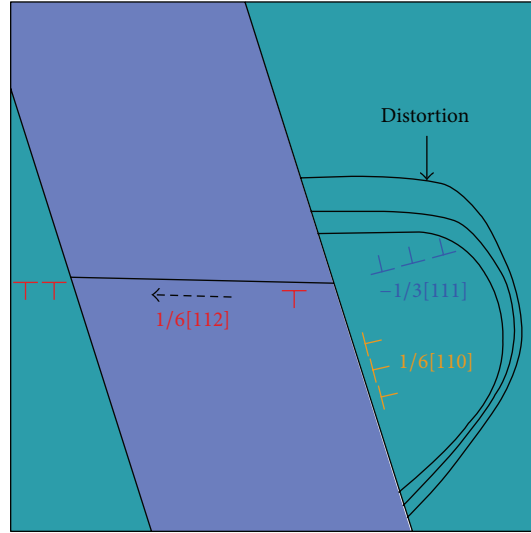


FIGURE 3: A schematic illustration of the reaction and movement of dislocations.

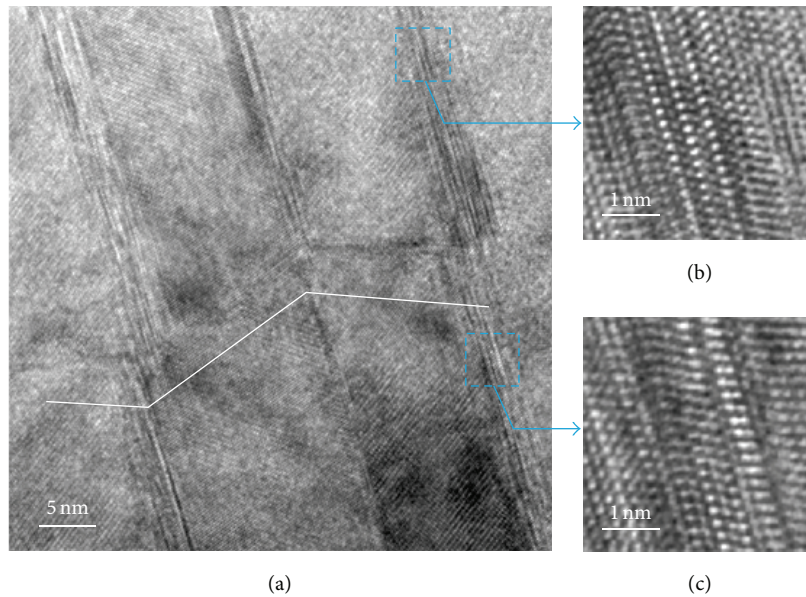


FIGURE 4: (a) A HRTEM graph of a ribbon of planar faults. (b) A magnified HRTEM graph of the upper γ/γ lath interface. (c) A magnified HRTEM graph of the lower γ/γ lath interface.

large, that the γ lath is deformed and the γ/γ lath interface is broken into two pieces. Considering this, lattice distortion can be observed on the γ/γ interface. Figures 4(b) and 4(c) show the lattice distortion upper and lower to the ribbon. As shown in Figure 3, the upper distortion is generated by $-1/3[111]$ partials, so it is perpendicular to the interface; the lower is generated by $1/6[110]$ partials, so it is parallel to the interface. As discussed above, $1/6[112]$ is the most common shear transformation on the $(11\bar{1})$ plane, and it could form SISF on the $(11\bar{1})$ plane. However, other shear transformations may also take place, that is, 2 times of 3 times of $1/6[112]$, and thus form more complicated planar faults.

After formation of the ribbon, shear transformation may further develop and more complicated substructure

could form. Figure 5 shows two major possible substructures: twin intersection and high concentration of planar faults. Figure 5(a) illustrates a SISF formed on the $(11\bar{1})$ plane. A $1/6[112]$ shear has already taken place to form the SISF, so it could act as nuclei for further shear transformation [13]. If the following shear is complete and homogeneous, secondary twin may form on the $(11\bar{1})$ plane. Yoo and Hishinuma [14] calculated that perfect secondary twin could form by homogeneous shear of $2/3[112]$, namely, 4 times of $1/6[112]$ shear transformation. The formation of secondary twin may cause lattice distortion inside the γ lath. This distortion may be accommodated by glide of perfect $1/2\langle 110 \rangle$ dislocations [6]. After formation of the secondary twin, it may penetrate into adjacent γ laths. Since the adjacent γ has a true twin

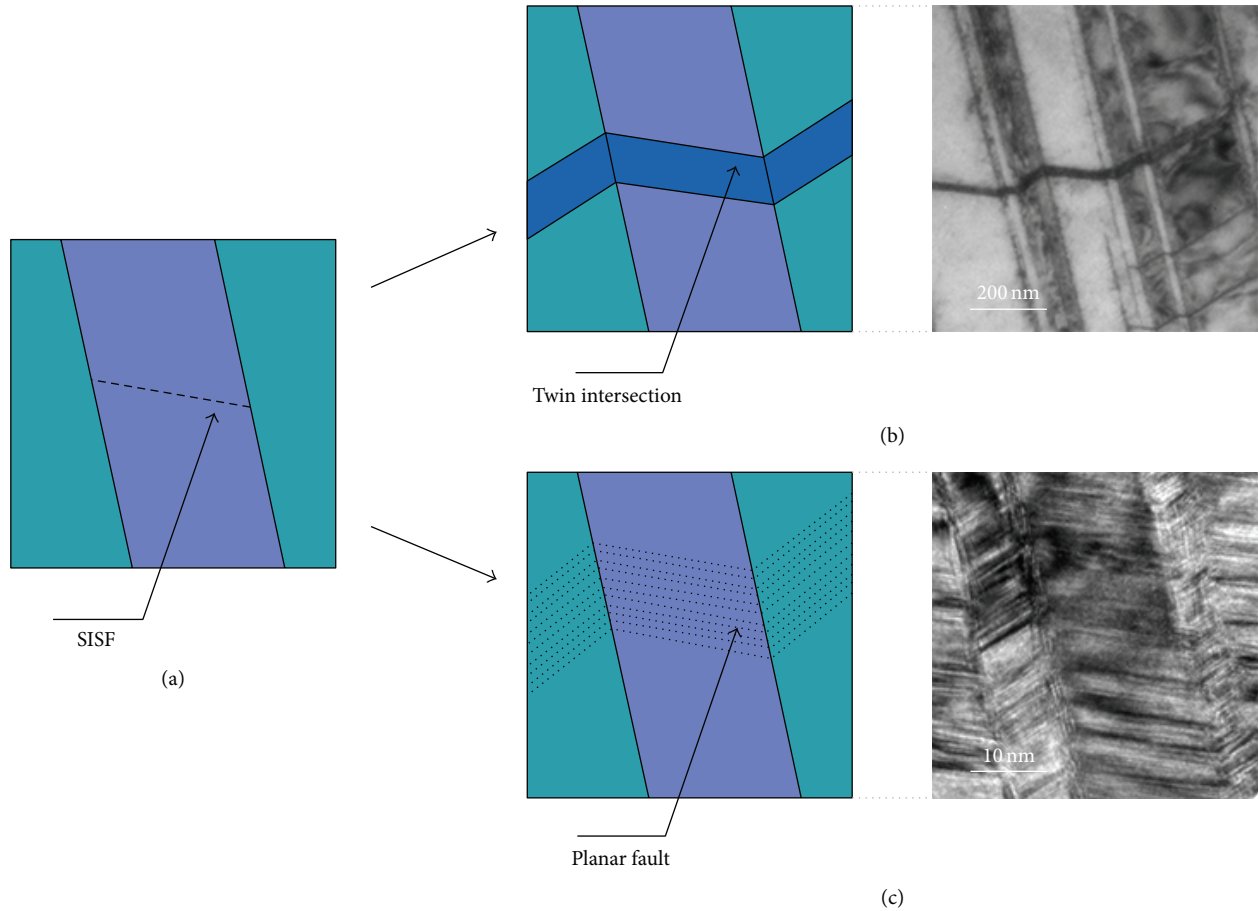


FIGURE 5: (a) A schematic illustration of a SISF formed inside a γ lath. (b) A schematic illustration and a TEM graph of the twin intersection. (c) A schematic illustration and a HRTEM graph of a high concentration of planar faults.

relationship with the original lath, the twinning system is totally changed. The original $1/6[112](11\bar{1})$ system becomes $1/18[5\bar{5}2](11\bar{5})$, which is immobile [15]. Because of this, the adjacent γ lath could provide an efficient barrier to the penetration of secondary twin, and the adjacent lath is thus called barrier twin [16]. Also, the growth of the secondary twin may be deflected at the twin interface, since twinning transformation takes place, and an intersection of twins thus forms. Figure 5(b) shows a schematic illustration and a TEM graph of the twin intersection.

If the shear transformation following the formation of SISF is incomplete or inhomogeneous, a high concentration of planar faults may form based on the SISF. As discussed above, the formation of secondary twin requires 4 times of $1/6[112]$ shear transformation. The 4 times of shear must act on the same $(11\bar{1})$ plane. If they act on different $(11\bar{1})$ planes, it could lead to formation of 4 SISFs. Also, shear of 2-3 times of $1/6[112]$ may also lead to planar faults. The formation of planar faults requires less shear transformation compared with the secondary twin, so the concentration of the planar fault is much higher than that of the secondary twin. The planar fault may also penetrate through the γ/γ lath interface. Because the formation of planar faults requires

less shear transformation, the penetration is much easier compared with the secondary twin, and the high concentration of penetrating planar faults can be also observed on the $(11\bar{1})$ plane of adjacent, twinning laths. The distortion caused by penetration distributes homogeneously on the γ/γ lath interface, so the over configuration of the interface is changed. It is not straight any more, but curved where the distortion is relatively strong. Figure 5(c) shows a schematic illustration and a TEM graph of the penetrating planar faults. As can be seen from the TEM graph, planar faults almost fill up the γ laths.

4. Summary

Shear transformation is a major mechanism for deformation mechanism for γ laths. In the current work, the shear transformation on the $(11\bar{1})$ plane of γ laths and its relative substructures are analyzed.

At the beginning of shear transformation, $1/6[112]$ Shockley partials are generated and SISF forms. As the shear transformation develops, the SISF can act as nuclei of more complex substructures. If the subsequent shear transformation is homogeneous and complete, secondary

twin could form. The secondary twin may penetrate the γ/γ lath interface and form a twin intersection. If the subsequent is inhomogeneous or incomplete, secondary could not form and planar faults form instead. The planar fault may also penetrate the γ/γ lath interface and engender planar faults on the $(11\bar{1})$ plane of adjacent γ laths.

Conflict of Interests

The authors declare that there is no conflict of interests regarding the publication of this paper.

Authors' Contribution

The authors claim that all authors have participated sufficiently in this work to take public responsibility for it. The authors claim that all authors have reviewed the final version of the paper and approve it for publication. The authors claim that neither this paper nor one with substantially similar content under our authorship has been published or is being considered for publication elsewhere.

References

- [1] Y.-W. Kim, "Ordered intermetallic alloys, part III: gamma titanium aluminides," *JOM*, vol. 46, no. 7, pp. 30–39, 1994.
- [2] H. Clemens and S. Mayer, "Design, processing, microstructure, properties, and applications of advanced intermetallic TiAl alloys," *Advanced Engineering Materials*, vol. 15, no. 4, pp. 191–215, 2013.
- [3] A. Denquin and S. Naka, "Phase transformation mechanisms involved in two-phase TiAl-based alloys—I. Lamellar structure formation," *Acta Materialia*, vol. 44, no. 1, pp. 343–352, 1996.
- [4] J. Schwerdtfeger and C. Körner, "Selective electron beam melting of Ti–48Al–2Nb–2Cr: microstructure and aluminium loss," *Intermetallics*, vol. 49, pp. 29–35, 2014.
- [5] Z. Jin and G. T. Gray III, "Experimental determination of domain orientations and domain orientation relationships across lamellar interfaces in polysynthetically twinned TiAl crystals," *Materials Science and Engineering A*, vol. 231, no. 1-2, pp. 62–71, 1997.
- [6] S. Wardle, I. Phan, and G. Hug, "Analysis of twin intersections in TiAl," *Philosophical Magazine A*, vol. 67, no. 2, pp. 497–514, 1993.
- [7] Y. Sun, P. Hazzledine, and J. Christian, "Intersections of deformation twins in TiAl II. Models and analyses," *Philosophical Magazine A*, vol. 68, no. 3, pp. 495–516, 1993.
- [8] Ch. Ricolleau, A. Denquin, and S. Naka, "High-resolution electron microscopy study of $\gamma - \gamma_T$ twin interfaces in the lamellar structure of TiAl-based alloys," *Philosophical Magazine Letters*, vol. 69, no. 4, pp. 197–204, 1994.
- [9] Nauka, Moscow, Russia, 1994.
- [10] J. W. Christian and S. Mahajan, "Deformation twinning," *Progress in Materials Science*, vol. 39, no. 1-2, pp. 1–157, 1995.
- [11] F. Appel, "An electron microscope study of mechanical twinning and fracture in TiAl alloys," *Philosophical Magazine*, vol. 85, no. 2-3, pp. 205–231, 2005.
- [12] D. Hull and D. J. Bacon, *Introduction to Dislocations*, Pergamon Press, Oxford, UK, 1984.
- [13] M. Kumar, S. Sriram, A. J. Schwartz, and V. K. Vasudevan, "Weak-beam analysis of dissociated $1/2 \llbracket 112 \rrbracket$ superdislocations in gamma-TiAl," *Philosophical Magazine Letters*, vol. 79, no. 6, pp. 315–325, 1999.
- [14] M. H. Yoo and A. Hishinuma, "Deformation twinning in TiAl: effects of defect clustering," *Metals and Materials International*, vol. 3, no. 2, pp. 65–74, 1997.
- [15] F. Appel, J. D. H. Paul, and M. Oehring, *Gamma Titanium Aluminide Alloys: Science and Technology*, Wiley, 2011.
- [16] F. Appel and R. Wagner, "Microstructure and deformation of two-phase γ -titanium aluminides," *Materials Science and Engineering R: Reports*, vol. 22, no. 5, pp. 187–268, 1998.

Research Article

A Study of Thin Film Resistors Prepared Using Ni-Cr-Si-Al-Ta High Entropy Alloy

Ruei-Cheng Lin,¹ Tai-Kuang Lee,² Der-Ho Wu,¹ and Ying-Chieh Lee³

¹Department of Mechanical Engineering, National Pingtung University of Science & Technology, Pingtung 91201, Taiwan

²Department of Electrical Engineering, National Cheng Kung University, Tainan 701, Taiwan

³Department of Materials Engineering, National Pingtung University of Science & Technology, Pingtung 91201, Taiwan

Correspondence should be addressed to Ying-Chieh Lee; ychee@mail.npust.edu.tw

Received 23 October 2014; Revised 29 November 2014; Accepted 28 December 2014

Academic Editor: Ke Fu Yao

Copyright © 2015 Ruei-Cheng Lin et al. This is an open access article distributed under the Creative Commons Attribution License, which permits unrestricted use, distribution, and reproduction in any medium, provided the original work is properly cited.

Ni-Cr-Si-Al-Ta resistive thin films were prepared on glass and Al₂O₃ substrates by DC magnetron cosputtering from targets of Ni_{0.35}-Cr_{0.25}-Si_{0.2}-Al_{0.2} casting alloy and Ta metal. Electrical properties and microstructures of Ni-Cr-Si-Al-Ta films under different sputtering powers and annealing temperatures were investigated. The phase evolution, microstructure, and composition of Ni-Cr-Si-Al-Ta films were characterized by X-ray diffraction (XRD), transmission electron microscopy (TEM), and Auger electron spectroscopy (AES). When the annealing temperature was set to 300°C, the Ni-Cr-Si-Al-Ta films with an amorphous structure were observed. When the annealing temperature was at 500°C, the Ni-Cr-Si-Al-Ta films crystallized into Al_{0.9}Ni_{4.22}, Cr₂Ta, and Ta₅Si₃ phases. The Ni-Cr-Si-Al-Ta films deposited at 100 W and annealed at 300°C which exhibited the higher resistivity 2215 μΩ-cm with -10 ppm/°C of temperature coefficient of resistance (TCR).

1. Introduction

Rapid technological advancements in many electronics industries, such as in the telecommunication and information, the aerospace, and the precision measurement sectors of industry, require the continuous development of electronic components to achieve higher precision, reliability, and integration [1]. Among these components, the resistor is one of the fundamental components and is primarily used in electronic circuits. In this respect, the demands for thin film resistors with low temperature coefficients of resistance (TCR) and high precision have been increasing dramatically in recent years [2–5].

The temperature coefficient of resistance (TCR) is an important technical parameter of thin film resistors. A high TCR will result in resistance value drifting and will consequently influence the accuracy of resistors as the temperature changes [6]. The main factors influencing the TCR include the sputtering process, annealing temperature, and film composition, whereas film composition plays a decisive role

among these three factors. Therefore, employing an appropriate method for depositing a suitable film composition is the key to obtaining high-resistance resistors with a low TCR.

Extensive and rapid development in high entropy alloy has been conducted since the recent years by Yeh et al. [7]. These alloys are defined to have five or more principal metallic elements, with the concentration of each element varying between 5% and 35%. It is generally found that high entropy alloys form simple solid solution structures (rather than many complex phases) at elevated temperatures because of large mixing entropies. The simple crystal structures possess many excellent properties [8], such as easy of nanoprecipitation, high hardness, and superior resistance to temper softening, wear, oxidation, and corrosion. The recent progress in HEAs, such as many new face-centered cubic (fcc) and body-centered cubic (bcc) HEAs and some high entropy bulk metallic glasses have been developed. They display an excellent mechanical response and good wear resistance at low and high temperatures, as well as good plastic behavior [9–12].

Ni-Cr thin films are employed in integrated circuits, where low noise, good power dissipation, and a near-zero temperature coefficient of resistance are important requirements. Several studies have reported on the deposition of Ni-Cr resistive films by thermal evaporation [13–16] and radio frequency (RF) sputtering, primarily for use as hybrid resistors [17, 18]. Extensive work has been reported on the control of the sheet resistance R_s and TCR of Ni-Cr resistors by doping the films with different impurities. If silicon is added to the alloys, Ni-Cr-Si thin film resistors with very low temperature coefficients of resistivity are obtained, but the alloy resistivities are not significantly increased [1]. In our previous study, the effects of aluminum addition and annealing on the microstructure and electrical properties of Ni-Cr-Si films have been reported [19]. The electrical resistivities of the Ni-Cr-Si-Al films were higher than those of the Ni-Cr-Si films annealed at temperatures below 400°C, and the annealed Ni-Cr-Si-Al films exhibited a TCR close to zero. However, aluminum element has lower melting point (660°C), which is not good for stability. The tantalum, with high melting point is at 3020°C, will be being beneficial for thermal stability of resistive thin films [20].

To obtain resistive thin films with high resistivity and a low TCR, the concept of high entropy alloy was introduced to investigate the Ni-Cr-Si-Al-Ta composition as thin film resistors based on previously study of Ni-Cr-Si-Al thin resistor [19]. The effects of sputtering power and annealing temperature on the phases and microstructural and electrical properties of Ni-Cr-Si-Al-Ta thin films were investigated.

2. Experimental Procedure

Ni-Cr-Si-Al-Ta thin films of 80 nm in thickness were deposited on the substrates using a DC magnetron cosputtering system having a sputtering rate of 5 nm/min. Ni_{0.35}-Cr_{0.25}-Si_{0.2}-Al_{0.2} and tantalum of diameter 76.2 mm were used as targets. The sputtering chamber was evacuated to a background pressure of 7×10^{-7} Torr by a cryopump, and then the sputtering gas Ar with a purity of 99.999% at flow of 60 sccm was introduced into the chamber using mass flow controllers, by which the working pressure was 4.3×10^{-3} Torr. Thin films deposited on glass plates at room temperature were subjected to electron probe microanalysis (EPMA) and X-ray diffraction (XRD) studies, while thin films on Al₂O₃ substrates (size: 25 mm²) were used for measuring the electrical properties. The DC power was adjusted at 100 W and 200 W, respectively. The as-deposited films were annealed at 250 to 500°C for 4 hours, with a heating rate of 5°C/min in air.

The sheet resistance R_s of the films was measured using the four-point probe technique, and the thickness t of the films was measured by FE-SEM (cross-section). The resistivity measured by the four-probe method was consistent with the resistivity obtained by the product of R_s and t . The TCR values of the Ni-Cr-Si-Al-Ta films were measured on thin long strips cleaved from the substrate. Electrical contacts to the two ends of the resistive strips were obtained by selectively coating the ends with sputtered Ag. The DC resistance of

the strips was measured on digit multimeter (HP 34401A) at different temperatures (25°C and 125°C). TCR of the Ni-Cr-Si-Al-Ta films was measured by the following relation:

$$\text{TCR} = \left[\left(\frac{\Delta R}{\Delta T} \right) \times \frac{1}{R} \right] \times 10^6 \text{ ppm/K.} \quad (1)$$

The composition of the deposited films was determined by Auger electron spectroscopy (AES). AES depth profiles were obtained in a PHI 550ESCA/SAM Auger microprobe (Physical Electronics, USA). The crystallinity of the films was analyzed by X-ray diffraction (XRD, Bruker D8A Germany), using Cu K α radiation for 2 θ values from 20° to 70°, with a scan speed of 3° min⁻¹ and a grazing angle of 0.5° at 40 kV and 40 mA. Microstructural and thickness observations of the cross-sectional and plane-view morphology of thin films grown on glass substrates were analyzed by field-emission scanning electron microscopy (FE-SEM, Hitachi S-4700 Japan) with an accelerating voltage of 20 kV. The microstructure of the films was also investigated by a field-emission transmission electron microscope (FE-TEM, FEI/O. Tecnai F20) equipped with an energy-dispersive spectrometer at an acceleration voltage of 200 kV. TEM specimens were prepared by disk cutting, mechanical polishing, dimpling, and ion milling. A Fischione 150 ultrasonic disk cutter (Fischione Instruments Inc., Export, PA) was used to cut a 3 mm sample, which was then mechanically polished to approximately 100 μ m in thickness using a diamond lapping film. The sample thickness during lapping was accurately controlled by a tripod polisher (SPI Supplies, West Chester, PA). Next, the polished sample was dimpled to a thickness of approximately 4 μ m using a Fischione 150 dimpling grinder, followed by ion milling on both sides with a Fischione 1010 ion miller to achieve an electron transparent thickness (<100 nm).

3. Results and Discussion

3.1. The Compositions, Phase Transformation, and Microstructure of the Sputtered Films. Electron probe microanalysis (EPMA) was used to determine the film compositions. The relative concentrations of nickel, chromium, silicon, aluminum, and tantalum were measured at three points in the sputtered films, respectively. The average values are listed in Figure 1. The results indicate that the composition of the sputtered Ni-Cr-Si-Al-Ta films with different sputtering powers were 23.5% Ni, 14.6% Cr, 23.6% Si, 16.8% Al, and 21.5% Ta at 100 W and 24.5% Ni, 13.8% Cr, 23.6% Si, 17.6% Al, and 20.5% Ta at 200 W, respectively. It was found that the Ta content was about 20%. However, these films are accorded to the rule of high entropy alloys which have five or more principal metallic elements with the concentration of each element varying between 5% and 35%.

Figure 2 shows X-ray diffraction patterns of Ni-Cr-Si-Al-Ta films at 200 W, for the as-deposited samples and those annealed at various temperatures for 240 min. All of the Ni-Cr-Si-Al-Ta films annealed at $\leq 400^\circ\text{C}$ exhibited an amorphous structure, indicating that none of the elements crystallized or oxidized. The term amorphous is a general term that refers to a solid state with a nonperiodical atomic

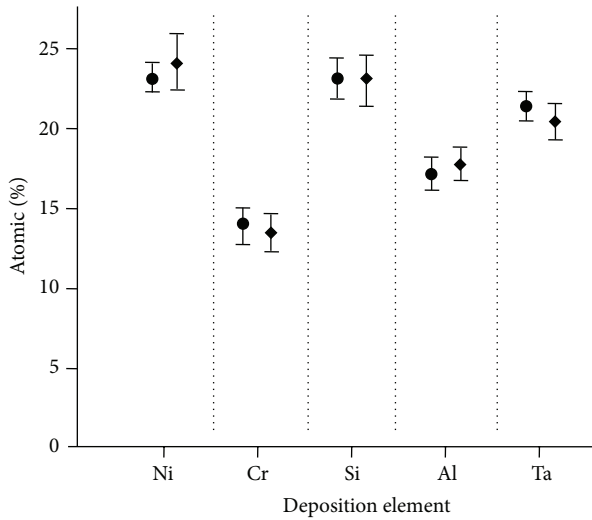


FIGURE 1: Compositions of Ni-Cr-Si-Al-Ta thin films with different DC sputtering powers sputtered on cooper sheet.

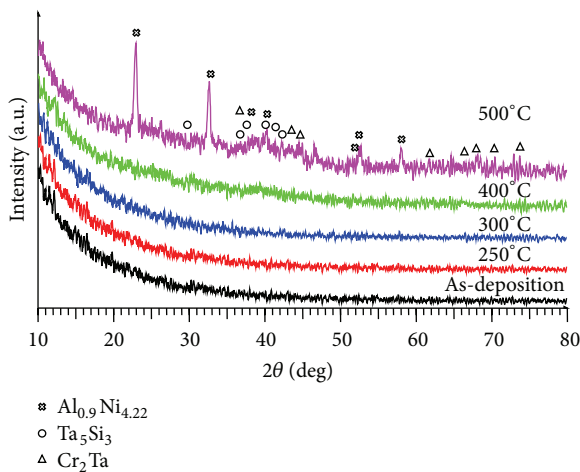


FIGURE 2: X-ray diffraction patterns of Ni-Cr-Si-Al-Ta thin films sputtered at 200 W with different annealing temperatures.

arrangement. A particular feature of an amorphous material at the atomic level in comparison with crystalline material is the absence of long-range order in the atoms. However, the atomic arrangement at the atomic scale (distance of a few diameters of atoms) is periodical [21]. The structure of crystalline materials can be easily determined by describing the unit cells of the crystals. The characterization of an amorphous structure is much more difficult due to the broadening of diffraction patterns and the lack of reflections during X-ray investigations. Further study is needed to use transmission electron microscopy for crystalline analysis. It is interesting to point out that the Ni-Cr-Si-Al-Ta films did not oxidize after 500°C annealing in air; there are only alloy phases formed in the Ni-Cr-Si-Al-Ta films. Yeh et al. [7, 22] reported that the HEAs can enhance the high temperature strength, corrosion, oxidation resistance, and so on.

Figure 3 shows X-ray diffraction patterns of Ni-Cr-Si-Al-Ta films with different sputtering powers on glass substrates, for as-deposited samples and those annealed at 500°C for 240 min. The figure shows that the as-deposited films had an amorphous structure. When the annealing temperature was set to 500°C, the crystallization of $\text{Al}_{0.9}\text{Ni}_{4.22}$, Ta_5Si_3 , and Cr_2Ta was clearly discernible. In Figure 3(b), which also shows the results at different sputtering power, the intensity of XRD peaks clearly increases with increasing sputtering power up to 200 W. It indicates that the crystalline film is strongly influenced by the sputtering power when the films annealed at high temperature. This may be attributed to the fact that, at high sputtering power, the ejected metal atoms possess higher kinetic energy when they arrive on the substrate [23]. Consequently, these Ni, Cr, Si, Al, and Ta atoms have sufficient kinetic energy to rearrange themselves to form closer packing layer, resulting in a highly nanocrystalline film structure. The numbers or energy of electrons and ions in glow discharge plasma will increase with an increment in sputtering powers, in the case of using metal target [24, 25]. That is, the energy of sputtered atom which is obtained from the positive ions colliding to target will increase with increasing sputtering power. It is also possible that the highly energized electrons with increasing sputtering power will bombard the surface of growing film at the substrate, providing in the form thermal energy. This energy might act as an additional energy to promote the growth of crystalline. Therefore, it can be concluded that as the sputtering power increases, the number and the momentum of the sputtering particles will also increase. The atoms become more mobile on the surface of the film as the result of the higher bombardment rates on them [26].

Figure 4 shows SEM micrographs of the Ni-Cr-Si-Al-Ta thin films with different sputtering powers and annealing temperatures. Some heterogeneous phases appeared after annealing at 400°C in the Ni-Cr-Si-Al-Ta thin films deposited at 200 W, as shown in Figure 4(b), and it obviously appeared after annealing at 500°C as shown in Figure 4(c), which is consistent with the XRD analysis (Figure 2). These crystal phases should belong to $\text{Al}_{0.9}\text{Ni}_{4.22}$, Ta_5Si_3 , and Cr_2Ta . For the Ni-Cr-Si-Al-Ta thin films deposited at 100 W and annealed at 500°C, the heterogeneous phases were also observed, as shown in Figure 4(d).

Figure 5 shows a typical TEM bright field image and selected-area electron diffraction (SAED) patterns of the Ni-Cr-Si-Al-Ta thin films with different sputtering powers and annealing temperatures. For Ni-Cr-Si-Al-Ta thin films deposited at 200 W and annealed at 300°C, it shows that the film with nanocrystalline structure appeared as shown in Figure 5(a). This result can be confirmed using the SAED patterns as shown in Figure 5(b). Therefore, the increase of sputtering power obviously causes the formation of a crystalline phase. With the annealing temperature increasing, more nanocrystallites were observed significantly to nucleate homogeneously throughout thin films and the SAED patterns changed to Debye-Scherrer-type rings (Figures 5(c) and 5(d)). However, the crystallites of the films annealed at 500°C were obviously larger than the films annealed at 300°C. The phase analysis performed from the electron

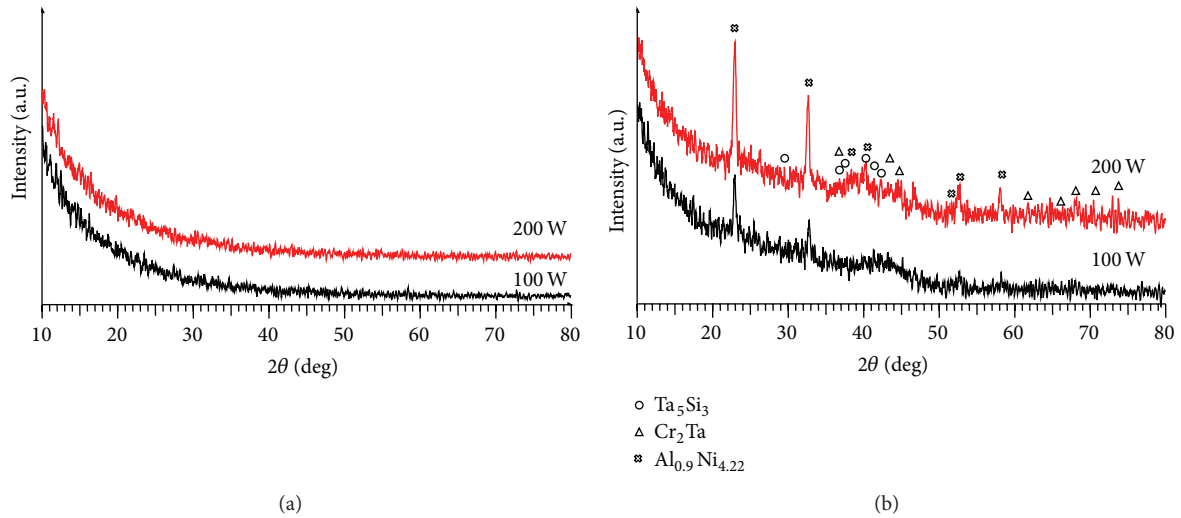


FIGURE 3: X-ray diffraction patterns of Ni-Cr-Si-Al-Ta thin films with different sputtering powers: (a) as-deposited and annealed at (b) 500°C.

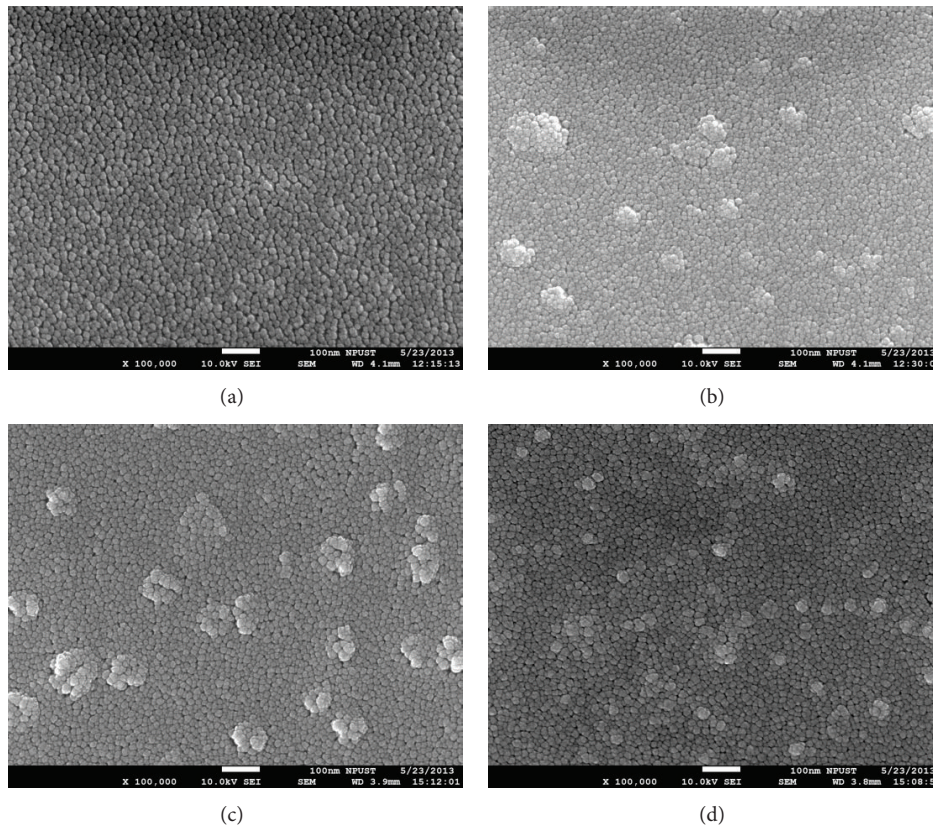


FIGURE 4: SEM micrographs of Ni-Cr-Si-Al-Ta films sputtered and annealed at (a) 200 W/300°C, (b) 200 W/400°C, (c) 200 W/500°C, and (d) 100 W/500°C.

diffraction patterns enables the identification of $\text{Al}_{0.9}\text{Ni}_{4.22}$ and Cr_2Ta phases. The increase in peak intensities indicates an enhancement in the crystallinity of films because it is generally noted that the crystallinity can be enhanced while increasing the annealing temperature [27, 28].

It is still of interest when considering phase competition between the solid solution phases and potential compounds (intermetallics). In other words, it is important to understand the thermodynamic nature of the phase stability of the solid solutions in Ni-Cr-Si-Al-Ta thin films at elevated

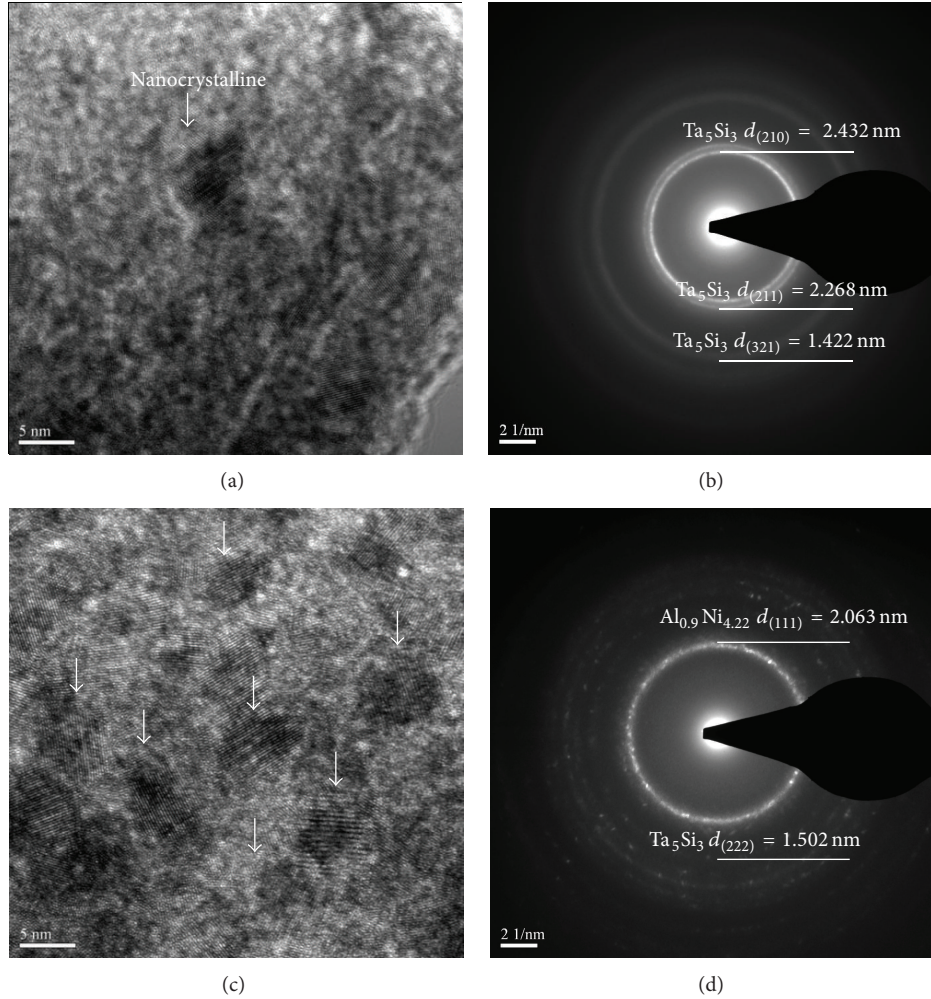


FIGURE 5: TEM micrographs and selected-area electron diffraction of Ni-Cr-Si-Al-Ta films sputtered and annealed at 200 W/300°C for (a) and (b) and 200 W/500°C for (c) and (d).

temperatures. Solid solutions are stable when the mixed crystal has lower free energy than the alternative-building up two crystals of different composition or building up a new structure in which the foreign atoms are put on ordered sites. The free energy is given by the following relation:

$$G = E + PV - TS, \quad (2)$$

where E is largely determined by the structural energy and the entropy is a measure of the randomness of the structure. If an atom added at random greatly increases the structure energy, the solid solution is unstable and two crystal structures form. On the other hand, if the addition of a foreign atom greatly lowers the structure energy, the system tends to form an ordered new phase. If the energy is not much changed, the entropy is increased by random additions so that the solid solution has the lowest energy and is the stable configuration [29].

3.2. The Electrical Properties of Ni-Cr-Si-Al-Ta Thin Films. To apply a material in thin film resistors, it is important to

know (i) the range of resistivity in which a near-zero TCR can be obtained and (ii) the detailed resistance behavior in the range of working temperatures (usually -55°C to 125°C) [30]. Figure 6 shows the effect of annealing temperature and sputtering power on the electrical properties of the Ni-Cr-Si-Al-Ta films. The resistivity of Ni-Cr-Si-Al-Ta films decreases obviously with increasing of annealing temperatures. This result indicates that atomic configuration changes have occurred in Ni-Cr-Si-Al-Ta films. It is interesting to point that the resistivities of the Ni-Cr-Si-Al-Ta films are different between 100 and 200 W of sputtering power at 300°C annealing. The resistivity of Ni-Cr-Si-Al-Ta films is ~ 2200 and $\sim 1600 \mu\Omega\text{-cm}$ for 100 W and 200 W, respectively. There is more than 35% difference in resistivity between them. The reason for this is due to different crystal structures of Ni-Cr-Si-Al-Ta films with different sputtering power at 300°C ; one is an amorphous at 100 W and the other one is nanocrystalline at 200 W. It is also interesting to note that the resistivity of the Ni-Cr-Si-Al-Ta films decreases with increasing the annealing temperature. From the above XRD and TEM results, the crystallinity of Ni-Cr-Si-Al-Ta films was enhanced

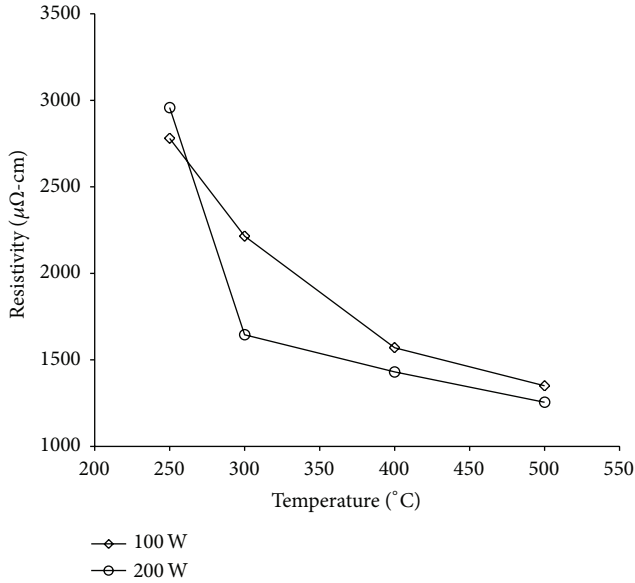


FIGURE 6: Room temperature resistivity of Ni-Cr-Si-Al-Ta films with different sputtering powers and annealing temperatures.

with increasing the annealing temperature. In general, by increasing the annealing temperature, the resistivity of Ni-Cr-Si-Al-Ta films increases since the grain boundaries, crystal defects, and oxides generation of the film were increased [6]. In this investigation, the resistivity was decreased which can be attributed to an increase in alloy phases ($\text{Al}_{0.9}\text{Ni}_{4.22}$, Ta_5Si_3 and Cr_2Ta) with increasing the annealing temperature, as shown in Figures 2 and 5. According to Matthiessen's rule, the resistivity of a continuous film is a cumulative effect of various electron scattering processes in the film. The resistivity ρ_T of the film is given by the following relation:

$$\rho_T = \rho_B + \rho_S + \rho_I, \quad (3)$$

where ρ_B , ρ_S , and ρ_I are contributions made to the total resistivity of the film due to scattering at ideal lattice (same as bulk), scattering at film surface (dependent on film thickness), and scattering at imperfections (grain boundaries and impurities), respectively.

Figure 7 shows the effect of annealing temperature and sputtering power on the temperature coefficient of resistivity (TCR) of the Ni-Cr-Si-Al-Ta films. The TCR values were increased with increasing of annealing temperature. TCR values were about 200 ppm/°C annealed below 300°C at 200 W. Moreover, the Ni-Cr-Si-Al-Ta films deposited at 100 W annealed at 300°C exhibit a TCR close to zero because the films retain an amorphous structure after annealing. However, the TCR values of the films annealed at 500°C are about 1000 ppm/°C. The TCR value becomes worse when the annealing temperature is increased. It can be explained that the annealing response of the TCR is the result of competition between a negative contribution from weak localization effects in the amorphous region and a positive contribution from crystalline phase grains [31]. For practical

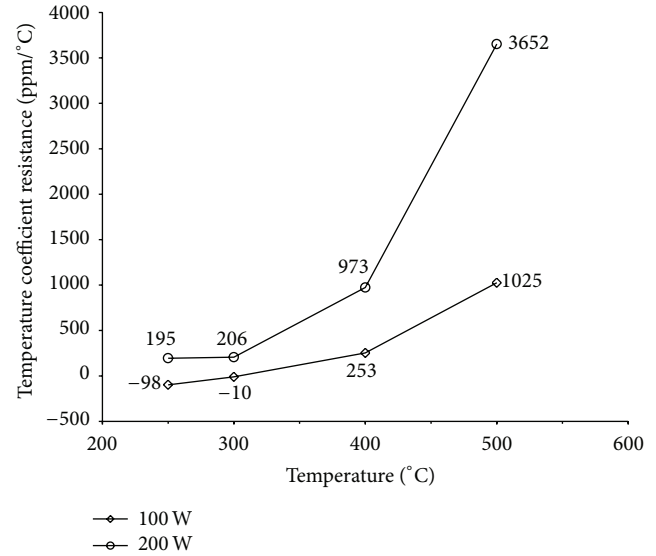


FIGURE 7: Temperature dependence of the TCR of Ni-Cr-Si-Al-Ta films with different sputtering powers and annealing temperatures.

purposes, it is important for films with a small TCR to possess high resistivity.

4. Conclusion

Ni-Cr-Si-Al (30/20/20/30 at.%) alloy and Ta targets were deposited on the glass and Al_2O_3 substrates as thin film resistor materials by cosputtering method. The compositions of film are accorded to the rule of high entropy alloys which have five elements with the concentration of each element varying between 5% and 35%. There is an amorphous structure observed in the films with sputtering power 100 W at 300°C. However, the annealing temperature was at 500°C; both films (100 W and 200 W) crystallized into $\text{Al}_{0.9}\text{Ni}_{4.22}$, Cr_2Ta , and Ta_5Si_3 phases. Electrical properties indicated that the Ni-Cr-Si-Al-Ta films with 100 W exhibited the smallest temperature coefficient of resistance (-10 ppm/°C) with higher resistivity $\sim 2200 \mu\Omega\text{-cm}$ after annealing at 300°C in air. For practical purposes, it is important for films with a small TCR to possess high resistivity. In this study, the introduction of HEAs concept can effectively enhance the electrical properties of Ni-Cr based thin films, satisfying the requirements for thin film resistor application.

Conflict of Interests

The authors declare that there is no conflict of interests regarding the publication of this paper.

Acknowledgment

The authors would like to acknowledge financial support of this research from the Ministry of Science and Technology of Taiwan under Contract no. 102-2221-E-020-008-MY3.

References

- [1] B.-J. Lee, D.-C. Lee, and C.-S. Kim, "Electrical properties of sputtered Ni-Cr-Al-Cu thin film resistors with Ni and Cr contents," *Journal of the Korean Physical Society*, vol. 40, no. 2, pp. 339–343, 2002.
- [2] A. P. Bhatt, C. A. Luck, and D. M. Stevenson, in *Proceedings of the International Symposium on Microelectronics*, p. 370, 1984.
- [3] K. Matsuda, K. Sato, T. Doi, K. Ogata, and K. Konishi, "Super precision metal film resistors," *National Technical Report*, vol. 26, pp. 283–288, 1980.
- [4] W. E. Isler and L. A. Kitchman, "Influence of deposition and processing parameters on the tcr of ni-cr-cu-al alloy film resistors," *IEEE Transactions on Parts, Materials and Packaging*, vol. 5, no. 3, pp. 139–146, 1969.
- [5] E. Schippel, "Modifications test of vacuum deposition Ni/Cr films with Mn and Si for thin film resistors," *Kristall und Technik*, vol. 15, no. 8, pp. 917–919, 1980.
- [6] X. Y. Wang, Z. S. Zhang, and T. Bai, "Investigation on powder metallurgy Cr-Si-Ta-Al alloy target for high-resistance thin film resistors with low temperature coefficient of resistance," *Materials and Design*, vol. 31, no. 3, pp. 1302–1307, 2010.
- [7] J. W. Yeh, S. K. Chen, S. J. Lin et al., "Nanostructured high-entropy alloys with multiple principal elements: novel alloy design concepts and outcomes," *Advanced Engineering Materials*, vol. 6, no. 5, pp. 299–274, 2004.
- [8] J.-W. Yeh, S.-K. Chen, J.-Y. Gan et al., "Formation of simple crystal structures in Cu-Co-Ni-Cr-Al-Fe-Ti-V alloys with multiprincipal metallic elements," *Metallurgical and Materials Transactions A: Physical Metallurgy and Materials Science*, vol. 35, no. 8, pp. 2533–2536, 2004.
- [9] C. Y. Hsu, J. W. Yeh, S. K. Chen, and T. T. Shun, "Wear resistance and high-temperature compression strength of Fcc CuCoNiCrAl_{0.5}Fe alloy with boron addition," *Metallurgical and Materials Transactions A*, vol. 35, no. 5, pp. 1465–1469, 2004.
- [10] O. N. Senkov, G. B. Wilks, J. M. Scott, and D. B. Miracle, "Mechanical properties of Nb₂₅Mo₂₅Ta₂₅W₂₅ and V₂₀Nb₂₀Mo₂₀Ta₂₀W₂₀ refractory high entropy alloys," *Intermetallics*, vol. 19, no. 5, pp. 698–706, 2011.
- [11] O. N. Senkov, S. V. Senkova, D. B. Miracle, and C. Woodward, "Mechanical properties of low-density, refractory multiprincipal element alloys of the Cr-Nb-Ti-V-Zr system," *Materials Science and Engineering A*, vol. 565, pp. 51–62, 2013.
- [12] F. Otto, A. Dlouhý, C. Somsen, H. Bei, G. Eggeler, and E. P. George, "The influences of temperature and microstructure on the tensile properties of a CoCrFeMnNi high-entropy alloy," *Acta Materialia*, vol. 61, no. 15, pp. 5743–5755, 2013.
- [13] D. S. Campbell and B. Hendry, "The effect of composition on the temperature coefficient of resistance of NiCr films," *The British Journal of Applied Physics*, vol. 16, no. 11, pp. 1719–1722, 1965.
- [14] J. G. Swanson, D. S. Campbell, and J. C. Anderson, "A study of electrical conduction in island structure nickel and 80:20 nickel-chromium films," *Thin Solid Films*, vol. 1, no. 5, pp. 325–342, 1968.
- [15] L. Lassak and K. Hieber, "Structural and electrical properties of evaporated Cr-Ni films as a function of gas pressure," *Thin Solid Films*, vol. 17, no. 1, pp. 105–111, 1973.
- [16] G. Nocerino and K. E. Singer, "The electrical and compositional structure of thin Ni-Cr films," *Thin Solid Films*, vol. 57, no. 2, pp. 343–348, 1979.
- [17] M. I. Birjega, C. A. Constantin, I. T. Florescu, and C. Sârbu, "Crystallization of amorphous sputtered 55%Cr–45%Ni thin films," *Thin Solid Films*, vol. 92, no. 4, pp. 315–322, 1982.
- [18] S. Schiller, U. Heisig, K. Goedicke et al., "Plasmatron sputtering for the production of high stability NiCr resistive films," *Thin Solid Films*, vol. 119, no. 2, pp. 211–216, 1984.
- [19] D.-J. Feng, Y.-C. Lee, and Y.-B. Chen, "A Study of Ni-Cr-Si-based thin film resistors prepared by DC magnetron sputtering," *International Journal of Materials Engineering and Technology*, vol. 11, no. 2, pp. 149–164, 2014.
- [20] S. Taioli, C. Cazorla, M. J. Gillan, and D. Alfè, "Melting curve of tantalum from first principles," *Physical Review B*, vol. 75, no. 21, Article ID 214103, 2007.
- [21] C. Ng, S. Guo, J. Luan, S. Shi, and C. T. Liu, "Entropy-driven phase stability and slow diffusion kinetics in an Al_{0.5}CoCrCuFeNi high entropy alloy," *Intermetallics*, vol. 31, pp. 165–172, 2012.
- [22] M.-H. Tsai and J.-W. Yeh, "High-entropy alloys: a critical review," *Materials Research Letters*, vol. 2, no. 3, pp. 107–123, 2014.
- [23] A. Anders, J. Andersson, and A. Ehiasarian, "High power impulse magnetron sputtering: current-voltage-time characteristics indicate the onset of sustained self-sputtering," *Journal of Applied Physics*, vol. 102, no. 11, Article ID 113303, 11 pages, 2007.
- [24] D.-J. Kwak, M.-W. Park, and Y.-M. Sung, "Discharge power dependence of structural and electrical properties of Al-doped ZnO conducting film by magnetron sputtering (for PDP)," *Vacuum*, vol. 83, no. 1, pp. 113–118, 2008.
- [25] N. Witit-Anun, J. Kaewkhao, and S. Chaiyakun, "Effect of sputtering power on structural and optical properties of ALN thin film deposited by reactive DC sputtering technique," *Advanced Materials Research*, vol. 770, pp. 177–180, 2013.
- [26] A. Chaoumead, Y.-M. Sung, and D.-J. Kwak, "The effects of RF sputtering power and gas pressure on structural and electrical properties of ITiO thin film," *Advances in Condensed Matter Physics*, vol. 2012, Article ID 651587, 7 pages, 2012.
- [27] M.-C. Jun and J.-H. Koh, "Effects of annealing temperature on properties of Al-doped ZnO thin films prepared by sol-gel dip-coating," *Journal of Electrical Engineering and Technology*, vol. 8, no. 1, pp. 163–167, 2013.
- [28] Z. Z. Zhi, Y. C. Liu, B. S. Li et al., "Effects of thermal annealing on ZnO films grown by plasma enhanced chemical vapour deposition from Zn(C₂H₅)₂ and CO₂ gas mixtures," *Journal of Physics D: Applied Physics*, vol. 36, no. 6, pp. 719–722, 2003.
- [29] X. Dong, J. Wu, and L. Mao, "The crystallization of Cr-Si-Ni-Al amorphous films-nucleation and growth of intermetallic phase Cr(Al,Si)₂," *Intermetallics*, vol. 11, no. 8, pp. 779–785, 2003.
- [30] J. Roelke, "Nichrome thin film technology and its application," *Electrocomponent Science and Technology*, vol. 9, no. 1, pp. 51–57, 1980.
- [31] S. Vinayak, H. P. Vyas, and V. D. Vankar, "Microstructure and electrical characteristics of Ni-Cr thin films," *Thin Solid Films*, vol. 515, no. 18, pp. 7109–7116, 2007.

Research Article

Fabrication of Fe-6.5wt%Si Ribbons by Melt Spinning Method on Large Scale

Y. F. Liang, S. Wang, H. Li, Y. M. Jiang, F. Ye, and J. P. Lin

State Key Laboratory for Advanced Metals and Materials, University of Science and Technology Beijing,
30 Xueyuan Road, Beijing 100083, China

Correspondence should be addressed to Y. F. Liang; liangyf@skl.ustb.edu.cn

Received 6 November 2014; Accepted 31 December 2014

Academic Editor: Jianfei F. Sun

Copyright © 2015 Y. F. Liang et al. This is an open access article distributed under the Creative Commons Attribution License, which permits unrestricted use, distribution, and reproduction in any medium, provided the original work is properly cited.

Melt spinning method has been widely applied for fabrication of Fe-based amorphous/nanocrystalline ribbons in industry. Compared with Fe-based amorphous/nanocrystalline alloys, Fe-6.5wt%Si high silicon steel is of low cost and has comparable excellent soft magnetic properties. Due to higher melting point and absence of supercooled liquid region, fabrication of Fe-6.5wt%Si ribbons is very hard and is only on lab scale. In this paper, we report that large scale fabrication of Fe-6.5wt%Si ribbons was successful and microstructures, ordered structures, and mechanical and soft magnetic properties of the ribbons were investigated. Due to rapid solidification rate, the ribbons were of ultrafine grains, and low degree of order and exhibited some extent of bending and tensile ductility. After heat treatment, excellent soft magnetic properties were obtained. Due to near-zero magnetostriction, the ribbons are promising to be used in electric devices with high frequencies where low noises are required.

1. Introduction

Fe-6.5wt%Si alloy has excellent soft magnetic properties [1], but it is very brittle at room temperature due to formation of ordered structures [2–4]. It is very hard to fabricate this alloy into thin sheet by conventional cold rolling method as cracks are easy to take place [5]. Warm and cold rolling method was developed to improve the ductility step by step during the process, but the whole process route was complex [6–8]. There are several other methods developed to avoid the room-temperature brittleness area, such as chemical vapor deposition (CVD) [9], spray forming [10, 11], direct powder rolling (DPR) [12], and dipping and diffusion annealing [13]. These methods have not succeeded in industry except JFE Super Cores produced by CVD process in Japan.

Rapid quenching from melt using single-roller has also been applied to produce Fe-6.5wt%Si alloy ribbons [14–17]. Small samples with width 5~25 mm were successfully obtained. Microstructure and mechanical and magnetic properties were investigated. Due to the limited size of the ribbon, rapid quenching has not succeeded in industry. Compared with amorphous Fe-based ribbons, Fe-6.5wt%Si alloy is much more difficult to be rapidly quenched into

continuous ribbons. Limitation of both width and length of the ribbons hinders the application of the melt spinning method. In this paper, we report successful fabrication of wide and continuous ribbons fabricated by melt spinning from single-roller. Ordered structures have crucial effect on mechanical and magnetic properties of this alloy and are investigated thereby.

2. Experimental

Raw materials of Fe-6.5wt%Si alloy were fabricated by melting electrolytic iron and metallic silicon together in a medium induction furnace in vacuum. For melt spinning, the alloy ingot was loaded in a quartz tube with a nozzle 30 mm long and melted by high-frequency induction heating. The molten alloy was ejected to a copper wheel with the aid of high pressure of argon in the quartz tube and the wide ribbons were formed with rapid solidification. A set of experimental conditions such as roller rotation speed, ejection pressure, and melting temperature were adjusted for production of continuous ribbons. Surfaces of the as-quenched ribbons were observed by scanning electron microscopy (SEM, Zeiss

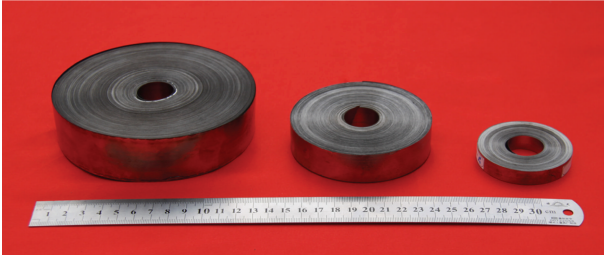


FIGURE 1: Melt spinning Fe-6.5wt%Si ribbons of $30\ \mu\text{m}$ in thickness, with width of 30 mm, 20 mm, and 10 mm from left to right.

SUPRA 55). Bending ductility was estimated by bending the ribbons to 180° and the longitudinal microstructure of the ribbon after bending was observed by optical microscopy (OM, Ernst Leitz Wetzlar). Ordered structures of the as-quenched ribbons were investigated by transmission electron microscopy (TEM, JEM-2010), for which a twin jet polishing in a solution of 90% glacial acetic acid and 10% perchloric acid was applied. A four-high mill was used for cold rolling of the as-quenched ribbons. Tensile tests were carried out using Instron 5969 tensile tester at room temperature with a strain rate of $10^{-3}\ \text{s}^{-1}$. AC magnetic properties were investigated followed by heat treatment of the as-quenched ribbon in vacuum and the MgO powder was used to prevent conglutination of the belt as reported previously [6].

3. Results and Discussion

The ribbons produced by single-roller melt spinning are shown in Figure 1, in which a continuous wound tape with 30 mm in height and 5 kg in weight is shown. The continuous ribbons have uniform edges, exhibiting good surface quality and metallic lustrous appearance. The thickness of the ribbons varies from 20 to $40\ \mu\text{m}$ mainly controlled by the distance from the nozzle to the Cu wheel when other parameters are fixed, such as the wheel speed, the air pressure, and the liquid temperature.

Direct observation of the surfaces of the as-quenched ribbons by SEM is shown in Figure 2. Ultrafine grains are obtained in the as-quenched ribbons, with diameters ranging from 0.5 to $5\ \mu\text{m}$. Due to the fast cooling and solidification rate, the crystal nucleation rate from the liquid is large, while the lateral growth of the crystals is prohibited.

The ribbons can be bent into certain shapes. No cracks are found in the bending area even after bending into 180° as shown in Figure 3. The excellent bending ductility guarantees that the ribbons can be coiled into tapes.

The microstructure of the ribbons after quenching is shown in Figure 4. From the diffraction pattern, it is found that the B2 spots exist, although the intensity is faint, while the D_{03} spots hardly exist. According to Figure 4(a), we can see that the formation of B2 ordered structure is hindered but not completely prohibited by rapid quenching, while, for D_{03} , the ordering transformation is completely prohibited during the rapid solidification process. Due to the spallation from the Cu wheel after rapid quenching, the ribbons are bent and

deformation takes place. In Figure 4(b), we can see that the super dislocations tangled and aligned.

Due to excellent ductility after rapid quenching, the ribbons can be cold rolled and the ribbons as-quenched and after cold rolling are shown in Figure 5, including surfaces of the ribbon, that is, the surface contacting Cu wheel and the free surface. After cold rolling, the roughness of the surface is improved, which is helpful to improve the lamination factor and thus the soft magnetic properties can be improved.

For the ribbons as-quenched and after cold rolling, the tensile engineering stress-strain curves are shown in Figure 6. It is found that the as-quenched ribbon exhibited excellent tensile ductility of about 1%, which is very good for this brittle alloy. After cold rolling, the yield stress increases with increasing rolling reduction, while the ductility of the ribbon decreases. Due to work hardening, the yield stress increases and the ductility decreases drastically.

After heat treatment ($1100^\circ\text{C}/5\ \text{h}$, furnace cooling), AC magnetic properties of the ribbons are shown in Figure 7 in comparison with ultrathin sheet produced by cold rolling [6] and CVD [18] methods. It is found that, with the frequencies below 10 kHz, the core losses in this work are a little higher or as good as those produced by cold rolling and CVD process. With frequencies larger than 10 kHz, the iron losses are much lower than cold rolled or CVD sheet. The core losses of ribbons are crucial to the thickness of the ribbon and also to their microstructure. Thinner thickness is helpful to decrease eddy current loss at high frequencies, and the melt spinning ribbons are more suitable to be used in high frequencies.

With proper control of melt spinning process, continuous ribbons with uniform edges are fabricated, exhibiting good surface quality, and can be coiled into large tapes. The thickness of the ribbons varies from 20 to $40\ \mu\text{m}$, and the width of the ribbons is up to 30 mm. Due to rapid cooling rate and thus rapid solidification rate, melt spinning ribbons are of ultrafine grains in lateral, with diameters ranging from 0.5 to $5\ \mu\text{m}$ as shown in Figure 2, while columnar grains are observed through the thickness of the ribbons, and the length could be $30\ \mu\text{m}$ as its thickness, as shown in Figure 3(b). Compared with the grain diameter of 10 mm for the 25 kg ingot, the grain size is decreased drastically. The rapid cooling rate is also helpful to hinder ordering transformations in this alloy. Room brittleness of this alloy is ascribed to the appearance of B2 and D_{03} ordered phases in this alloy [3, 5]. At higher temperatures, the alloy is of A2 structure and is rather ductile to be hot rolled. Single-roller rapid quenching is helpful to hinder transformation from A2 to B2 and prohibit ordering transformation from B2 to D_{03} , for which transformations take place at 750°C and 600°C , respectively [19]. As the brittleness is originating from the ordered structures in this alloy, especially from the mixture of B2 and D_{03} ordered structures, rapid quenching is helpful to improve the ductility. Bending and tensile experiments as shown in Figures 3, 5, and 6 indicate that the as-quenched ribbons have excellent room-temperature ductility and that the ribbons could be bent to 180° without bending cracks, could be cold rolled to 35% in reduction, and could be plastically deformed by tension. The excellent ductility of the ribbons guarantees that the continuous rapidly

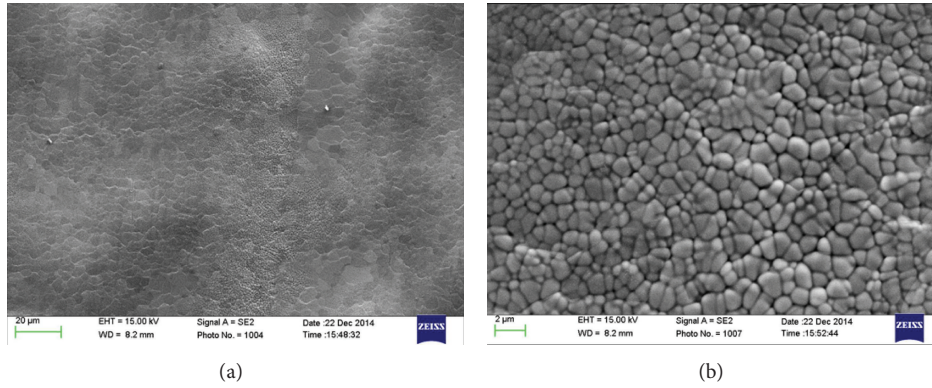


FIGURE 2: Surfaces of the ribbons after rapid quenching: (a) grain diameters of about 5 μm and (b) grain diameters of about 0.5 μm .

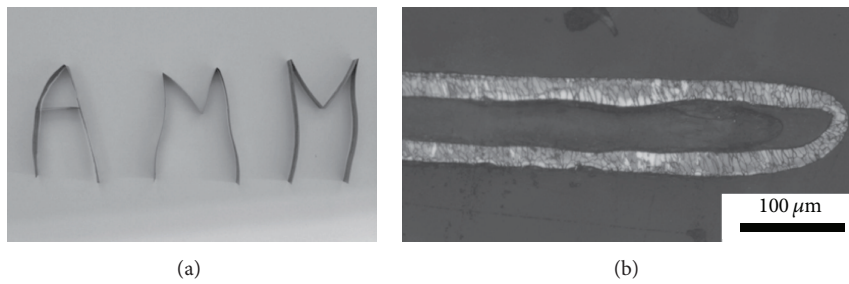


FIGURE 3: Rapidly quenched ribbons possess good bending ductility: (a) ribbons are bent into 180° and (b) no cracks are found after bending.

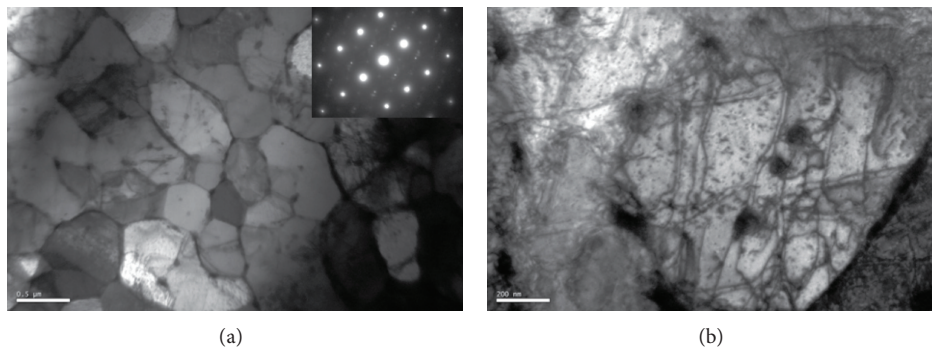


FIGURE 4: TEM of rapidly quenched ribbons: (a) bright field microstructure of the ribbon with diffraction pattern inset and (b) substructure of the ribbon showing super dislocations.

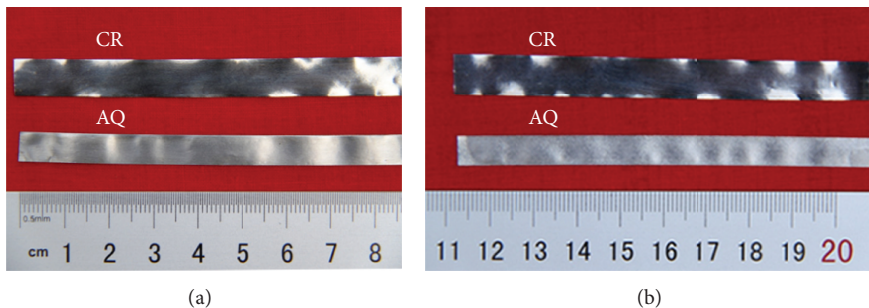


FIGURE 5: Rapidly quenched ribbons with and without cold rolling of 33% reduction: (a) surface contacting the single-roller and (b) free surface of the ribbon. AQ: as-quenched, CR: cold rolled.

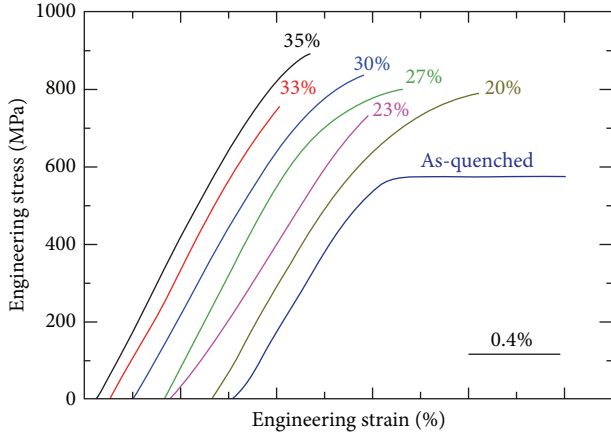


FIGURE 6: Tensile engineering stress-strain curves of as-quenched ribbon and ribbons with different cold rolling reduction.

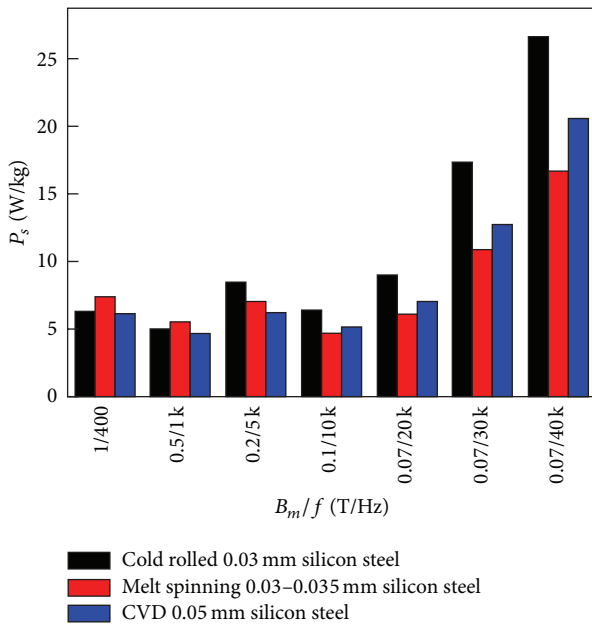


FIGURE 7: Core losses of rapidly quenched ribbons after heat treatment in comparison with cold rolled sheet and CVD sheet.

quenched ribbons could be coiled into tapes on large scale. After heat treatment, the rapidly quenched ribbons show as good soft magnetic properties as ultrathin sheet produced by cold rolling and CVD process and even better soft magnetic properties for higher frequencies up to 10 kHz.

4. Conclusions

- (1) Fabrication of Fe-6.5wt%Si ribbons with 30 mm in width was successful using single-roller rapid quenching method. The continuous ribbons have uniform edges, exhibit good surface quality, and can be coiled into large scale tapes.

- (2) Due to rapid solidification rate, ultrafine grains are obtained after melt spinning. Meanwhile, transformation of ordered structure B2 is hindered, and the ordered structure D0₃ is prohibited. The as-quenched ribbons exhibit excellent bending and tensile ductility.

- (3) After proper heat treatment, excellent AC magnetic properties can be obtained for as-quenched ribbons, comparable to ultrathin sheet fabricated by cold rolling or CVD process.

Conflict of Interests

The authors declare that there is no conflict of interests regarding the publication of this paper.

Acknowledgments

Financial support from the Major State Basic Research Development Program of China (973 Program, no. 2011CB606304), the Natural Science Foundation of China (no. 51301019), the Fundamental Research Funds for the Central Universities (no. FRF-TP-14-099A2), and the State Key Laboratory for Advanced Metals and Materials (no. 2014Z-23) is gratefully acknowledged.

References

- [1] R. M. Bozorth, *Ferromagnetism*, D. Van Nostrand, New York, NY, USA, 1951.
- [2] K. Raviprasad and K. Chattopadhyay, "The influence of critical points and structure and microstructural evolution in iron rich Fe-Si alloys," *Acta Metallurgica et Materialia*, vol. 41, no. 2, pp. 609–624, 1993.
- [3] J. S. Shin, J. S. Bae, H. J. Kim et al., "Ordering-disordering phenomena and micro-hardness characteristics of B2 phase in Fe-(5–6.5%)Si alloys," *Materials Science and Engineering A*, vol. 407, no. 1-2, pp. 282–290, 2005.
- [4] T. Ros-Yanez, D. Ruiz, J. Barros, Y. Houbaert, and R. Colás, "Study of deformation and aging behaviour of iron-silicon alloys," *Materials Science and Engineering: A*, vol. 447, no. 1-2, pp. 27–34, 2007.
- [5] J.-S. Shin, Z.-H. Lee, T.-D. Lee, and E. J. Lavernia, "The effect of casting method and heat treating condition on cold workability of high-Si electrical steel," *Scripta Materialia*, vol. 45, no. 6, pp. 725–731, 2001.
- [6] Y. F. Liang, F. Ye, J. P. Lin, Y. L. Wang, and G. L. Chen, "Effect of annealing temperature on magnetic properties of cold rolled high silicon steel thin sheet," *Journal of Alloys and Compounds*, vol. 491, no. 1-2, pp. 268–270, 2010.
- [7] Y. F. Liang, F. Ye, J. P. Lin, Y. L. Wang, L. Q. Zhang, and G. L. Chen, "Effect of heat treatment on mechanical properties of heavily cold-rolled Fe-6.5wt%Si alloy sheet," *Science China Technological Sciences*, vol. 53, no. 4, pp. 1008–1011, 2010.
- [8] F. Ye, Y. F. Liang, Y. L. Wang, J. P. Lin, and G. L. Chen, "Fe-6.5wt%Si high silicon steel sheets produced by cold rolling," in *Thermec 2009*, T. Chandra, N. Wanderka, W. Reimers, and M. Ionescu, Eds., parts 1–4, pp. 1428–1433, Trans Tech, Zürich, Switzerland, 2010.

- [9] Y. Takada, M. Abe, S. Masuda, and J. Inagaki, "Commercial scale production of Fe-6.5 wt. % Si sheet and its magnetic properties," *Journal of Applied Physics*, vol. 64, no. 10, pp. 5367–5369, 1988.
- [10] M. C. A. Silva, C. Bolfarini, and C. S. Kiminami, "Microstructure and magnetic properties of Fe-6.5wt%Si alloy obtained by spray forming process," *Materials Science Forum*, vol. 498-499, pp. 111–118, 2005.
- [11] C. Bolfarini, M. C. A. Silva, A. M. Jorge Jr., C. S. Kiminami, and W. J. Botta, "Magnetic properties of spray-formed Fe-6.5%Si and Fe-6.5%Si-1.0%Al after rolling and heat treatment," *Journal of Magnetism and Magnetic Materials*, vol. 320, no. 20, pp. e653–e656, 2008.
- [12] R. Li, Q. Shen, L. Zhang, and T. Zhang, "Magnetic properties of high silicon iron sheet fabricated by direct powder rolling," *Journal of Magnetism and Magnetic Materials*, vol. 281, no. 2-3, pp. 135–139, 2004.
- [13] T. Ros-Yañez, Y. Houbaert, and V. Gómez Rodríguez, "High-silicon steel produced by hot dipping and diffusion annealing," *Journal of Applied Physics*, vol. 91, no. 10, pp. 7857–7859, 2002.
- [14] K.-I. Arai and N. Tsuya, "Ribbon-form silicon-iron alloy containing around 6.5 percent silicon," *IEEE Transactions on Magnetism*, vol. 16, no. 1, pp. 126–129, 1980.
- [15] K. I. Arai, N. Tsuya, K. Ohmori, H. Shimanaka, and T. Miyazaki, "Rapidly quenched ribbon-form silicon-iron alloy with high silicon concentration," *Journal of Magnetism and Magnetic Materials*, vol. 15–18, no. 3, pp. 1425–1426, 1980.
- [16] J. E. Wittig and G. Frommeyer, "Deformation and fracture behavior of rapidly solidified and annealed iron-silicon alloys," *Metallurgical and Materials Transactions A*, vol. 39, no. 2, pp. 252–265, 2008.
- [17] R. K. Roy, A. K. Panda, M. Ghosh, A. Mitra, and R. N. Ghosh, "Effect of annealing treatment on soft magnetic properties of Fe-6.5 wt% Si wide ribbons," *Journal of Magnetism and Magnetic Materials*, vol. 321, no. 18, pp. 2865–2870, 2009.
- [18] Y. Tanaka, Y. Takada, M. Abe, and S. Masuda, "Magnetic properties of 6.5% Si-Fe sheet and its applications," *Journal of Magnetism and Magnetic Materials*, vol. 83, no. 1–3, pp. 375–376, 1990.
- [19] H. Okamoto, *Desk Handbook: Phase Diagrams for Binary Alloys*, ASM International, Materials Park, Ohio, USA, 2000.

Research Article

The Microstructures and Electrical Resistivity of (Al, Cr, Ti)FeCoNiO_x High-Entropy Alloy Oxide Thin Films

Chun-Huei Tsau,¹ Zhang-Yan Hwang,¹ and Swe-Kai Chen²

¹Graduate School of Nanomaterials, Chinese Culture University, Taipei 111, Taiwan

²Materials Science Center, National Tsing Hua University, Hsinchu 300, Taiwan

Correspondence should be addressed to Chun-Huei Tsau; chtsau@staff.pccu.edu.tw

Received 6 November 2014; Revised 9 December 2014; Accepted 9 December 2014

Academic Editor: Yong Zhang

Copyright © 2015 Chun-Huei Tsau et al. This is an open access article distributed under the Creative Commons Attribution License, which permits unrestricted use, distribution, and reproduction in any medium, provided the original work is properly cited.

The (Al, Cr, Ti)FeCoNi alloy thin films were deposited by PVD and using the equimolar targets with same compositions from the concept of high-entropy alloys. The thin films became metal oxide films after annealing at vacuum furnace for a period; and the resistivity of these thin films decreased sharply. After optimum annealing treatment, the lowest resistivity of the FeCoNiO_x, CrFeCoNiO_x, AlFeCoNiO_x, and TiFeCoNiO_x films was 22, 42, 18, and 35 μΩ-cm, respectively. This value is close to that of most of the metallic alloys. This phenomenon was caused by delaminating of the alloy oxide thin films because the oxidation was from the surfaces of the thin films. The low resistivity of these oxide films was contributed to the nonfully oxidized elements in the bottom layers and also vanishing of the defects during annealing.

1. Introduction

This study deals with the room-temperature resistivity of alloy oxide thin films. In our previous study on the high-entropy alloy, TiFeCoNiO_x film had an extremely low resistivity (~35 μΩ-cm) at room temperature [1, 2]. The value is almost close to that of metallic alloy, and it broke our concept that the alloy oxides had higher resistivity. Because the conductivity of semiconductors is much less than that of most metals, their resistivity was in the range between 10⁵ and 10¹⁴ μΩ-cm [3–5]. The design of the alloy targets of this study exploits Professor Yeh's equimolar alloy concept. Professor Yeh introduced the new concept of high-entropy alloys as basis for alloys whose properties are not dominated by their major element [6–12]. We used this concept to cast the TiFeCoNi alloy and studied its characteristics [13]; also we used this alloy as the target to measure the resistivity of the TiFeCoNiO_x thin film. In this study, we investigated the FeCoNiO_x, AlFeCoNiO_x, and CrFeCoNiO_x alloy oxide films, and the results were compared with TiFeCoNiO_x films. The FeCoNiO_x film was studied for estimating the effect of absence of titanium content. Additionally, we used aluminum to substitute titanium and studied AlFeCoNiO_x film, because

the elements of aluminum and titanium had similar activity [14]. We also added chromium to substitute titanium because of its excellent oxidation resistance.

2. Experimental Procedures

The FeCoNi, CrFeCoNi, AlFeCoNi, and TiFeCoNi alloys (named as FCN, CFCN, AFCN, and TFCN, resp.) were prepared by arc melting using appropriate amounts of titanium, aluminum, chromium, iron, cobalt, and nickel, the purity of all of which exceeded 99.9%. Table 1 lists the compositions of the targets analyzed by inductively coupled plasma atomic emission spectrometry (ICP-AES, Jarrell-Ash, ICAP 9000). DC physical vapor sputtering (PVD) was used to deposit these metallic films. It was performed at 100 W and the flow rate of Ar was 30 standard cubic centimeters per min (sccm). The base and working pressures were 5 × 10⁻⁵ and 2 × 10⁻³ torr, respectively. Some of the samples were annealed using a vacuum furnace with a mechanical pump, and the working pressure was 1 × 10⁻² torr. The microstructural evolutions of the thin films were monitored using scanning electron microscopy (SEM) and transmission electron microscopy (TEM). SEM observations were made using

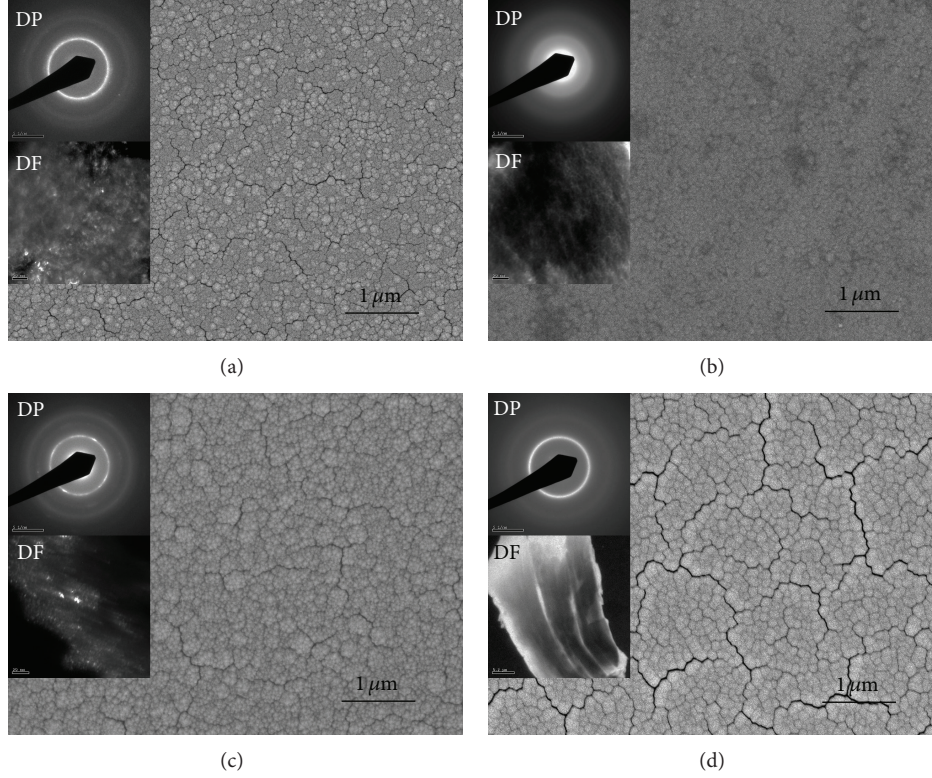


FIGURE 1: The plan-view micrographs of the as-deposited (a) FCN film; (b) CFCN film; (c) AFCN film; and (d) TFCN film, respectively. The insets are the corresponding SAD (marked by DP) and DF image (marked by DF) of each as-deposited thin film.

TABLE 1: The chemical compositions of the (Al, Cr, Ti)FeCoNi targets.

Alloys	Compositions (at.%)					
	Al	Ti	Cr	Fe	Co	Ni
FeCoNi	*	*	*	33.2	33.3	33.5
AlFeCoNi	24.8	*	*	25.2	25.1	24.9
TiFeCoNi	*	25.1	*	25.2	24.7	25.0
CrFeCoNi	*	*	25.1	24.8	25.3	24.8

a JEOL JSM-6335 field emission scanning electron microscope operated at 15 kV. TEM observations were made using a JEOL JEM-2010 transmission electron microscope operated at 200 kV. The room-temperature electrical resistivity of all samples was measured with a Napson Corporation Model TR-70 four-point probe.

3. Results and Discussion

The micrographs of the as-deposited alloy thin films are shown in Figure 1. The plan-view micrographs of the as-deposited alloy films all have a similar granular morphology. However, these structures are analyzed as an amorphous one, and the narrower black lines are amorphous grain boundaries. Donovan and Heinemann first observed these amorphous grain boundaries in an evaporated amorphous Ge thin film [15], and they suggested that the formation of

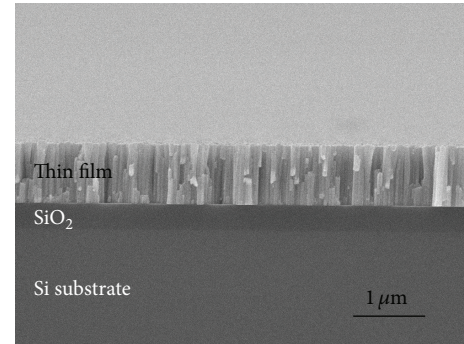


FIGURE 2: The cross section micrograph of the as-deposited FCN film which shows the typical columnar structure.

a void network resulted in density-deficient boundaries that are intrinsic to amorphous films. Tsukimoto et al. further described the mechanism of formation of amorphous grain boundaries in TaN thin films, following a detailed analysis [16]. In this study, the thin films also had a similar phenomenon; the typical cross section of these thin films all had the columnar structure, shown in Figure 2. The insets of each SEM micrograph, shown in Figure 1, are the corresponding selection area diffraction pattern (SAD) and TEM dark field image (DF), respectively. The SADs proved the amorphous structures, and the DF images show the nanoscale clusters in these thin films, indicating that the as-deposited thin films

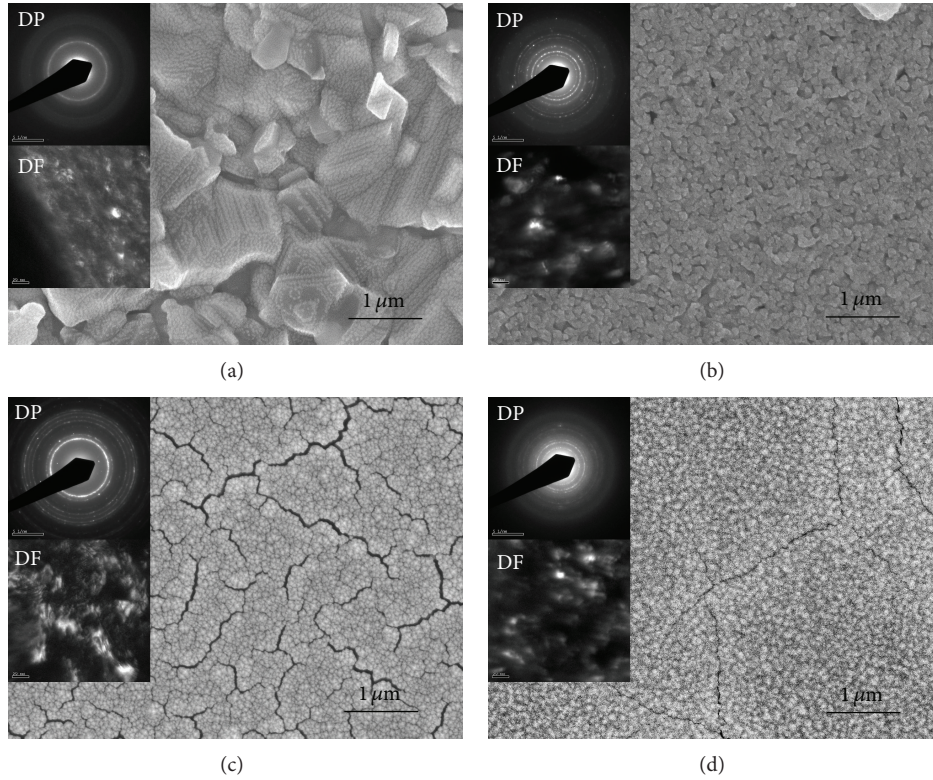


FIGURE 3: The plan-view micrographs of the as-annealed (a) FCN film; (b) CFCN film; (c) AFCN film; and (d) TFCN film, respectively. The insets are the corresponding SAD (marked by DP) and DF image (marked by DF) of each as-annealed thin film.

were not crystalline in structure. In addition, we observed the cracks on the surface of the as-deposited FCN, AFCN, and TFCN films, but no crack was observed in as-deposited CFCN film. The wide black lines in the SEM micrographs of the as-deposited thin films are the crack along the amorphous grain boundaries. These cracks were caused by the internal stress during the deposition process and the difference in atomic sizes. However, CoCrFeNi has single-phase solid solution, a ductile material with low hardness, and very similar atomic sizes [17, 18]. Therefore, no crack was found in this alloy thin film under as-deposited state.

These thin films became oxides after annealing at vacuum furnace at high temperature; and their morphologies also changed because of diffusion of the elements and oxidation. The plan-view of as-annealed micrographs of the FeCoNiO_x , CrFeCoNiO_x , AlFeCoNiO_x , and TiFeCoNiO_x films (named as FCNO, CFCNO, AFCNO, and TFCNO, resp.) is shown in Figure 3. The annealing conditions are all fixed at 1000°C for 30 min. The large granular structure of the FCNO film is quite different with as-deposited morphology, shown in Figure 3(a). The CFCNO film has a particle-like structure, shown in Figure 3(b). The cracks in the AFCNO film are wider than the as-deposited condition, shown in Figure 3(c). On the contrary, the cracks in the TFCNO film are less than as-deposited state, because of the crystallization and healing of voids and cracks along amorphous grain boundaries, shown in Figure 3(d). The columnar structures of the as-deposited thin films also changed after annealing. Figure 4

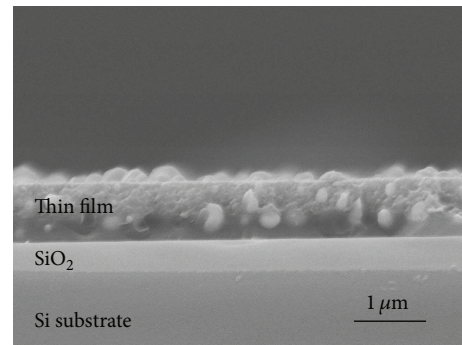


FIGURE 4: The cross section micrograph of the as-annealed AFCN thin film.

shows the cross section morphology of the CFCNO film after annealing at 1000°C for 30 min, indicating this thin film became a particle-like structure. The similar result was also observed in the other three thin films.

The resistivity of these four oxide films after vacuum annealing at different temperatures is shown in Figure 5. The annealing times were all fixed at 30 min. The resistivities of the as-deposited TFCN, FCN, AFCN, and CFCN films are 1860 , 950 , 175 , and $98 \mu\Omega\text{-cm}$, respectively. The as-deposited CFCN thin film had the lowest resistivity because of its uniform morphology; no crack was observed. All of these were because of their similar atomic sizes and less lattice

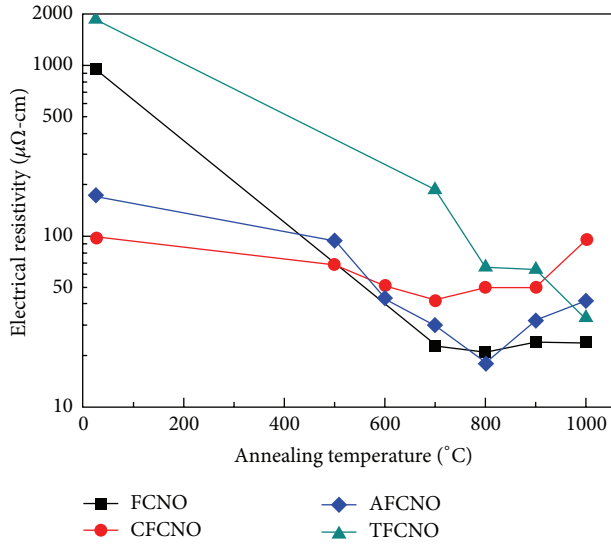


FIGURE 5: Plot of the resistivity of the thin films versus annealing temperature. The annealing times were all 30 min.

distortion [17, 18]. The other three as-deposited thin films all show that the cracks are along their amorphous grain boundaries. Therefore, the resistivity increased because of the defect. The resistivity of the thin films all decreased after annealing because of recrystallizing and eliminating of defects. We found this interesting phenomenon first in the TFCNO film; the resistivity of as-annealed TFCNO film was lower than that of the TiFeCoNi bulk alloy [1, 2]. Therefore, we further designed the other alloys to study this phenomenon. The resistivity of the TFCNO film decreased when the annealing temperature increased, and the lowest resistivity of the TFCNO was $35 \mu\Omega\text{-cm}$ after annealing at 1000°C for 30 min. The resistivity of the FCNO film also decreased after annealing, and the resistivity almost kept the same value ($\sim 23 \mu\Omega\text{-cm}$) at the annealing temperature range of $700\sim 1000^\circ\text{C}$ for 30 min. However, the FCNO film would be easily peeled off from the substrate if the annealing temperatures were not higher than 800°C . The thin film would slightly react with the SiO_2 layer of substrate and increase their bonding under high temperature annealing. The as-deposited AFCN films had lower resistivity, and its resistivity also decreased after annealing. The lowest resistivity of the AFCNO film was $18 \mu\Omega\text{-cm}$ after annealing at 800°C for 30 min; but the resistivity of AFCNO film increased if the annealing temperature was higher than 800°C . This study also observed the aluminum-oxide rich phase on the surface after annealing at 500°C for 30 min. Therefore, each thin film had its suitable annealing condition to get the lowest resistivity. The as-deposited CFCNO film had the lowest resistivity of $98 \mu\Omega\text{-cm}$; its resistivity only slightly decreased after annealing. The lowest resistivity of the CFCNO film was $42 \mu\Omega\text{-cm}$ after annealing at 700°C for 30 min.

According to the resistivity of the thin films described above, this study chose the annealing temperatures for the FCNO, TFCNO, CFCNO, and AFCNO thin film for investigating their resistivity aging curves which were 1000°C ,

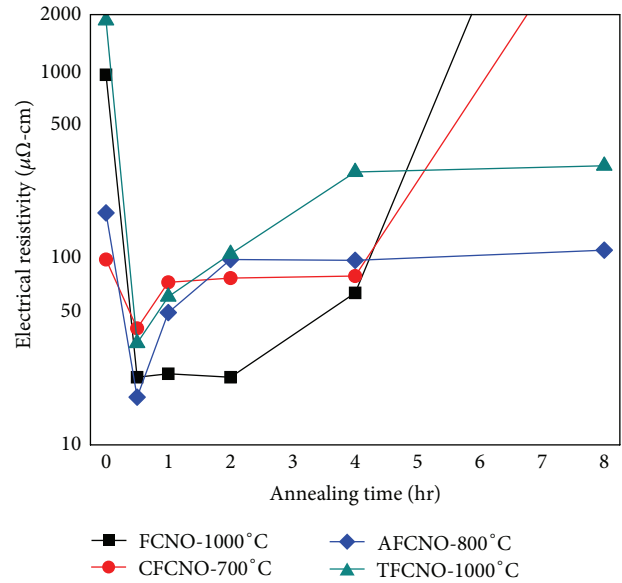


FIGURE 6: Plot of the resistivity of the thin films versus annealing times. The annealing temperatures for the FCNO, TFCNO, CFCNO, and AFCNO thin film were 1000°C , 1000°C , 700°C , and 800°C , respectively.

1000°C , 700°C , and 800°C , respectively. The relationship between the resistivity of the thin films and the annealing times is plotted in Figure 6. All of the curves indicate that the appropriate annealing time for the thin films is 30 min at these annealing temperatures. The lowest resistivity for each thin film was got under this annealing temperature. However, the appropriate annealing times for the thin films depended on the annealing temperature. The resistivity for the thin films increases after annealing for more than 30 min. The resistivity of the FCNO thin film almost kept the same value when the annealing time was less than 2 hours; and its resistivity increased sharply after annealing at 1000°C for more than 4 hours. The resistivity of the CFCNO thin film was worse than the FCNO thin film. The oxidation resistance of the CFCNO film had not been promoted after adding chromium; and its resistivity increased significantly after annealing at 700°C for more than 4 hours. The resistivity of TFCNO films indicated that the TFCNO film had attained very low resistivity level after annealing at 1000°C for 30 min. Additionally, its resistivity increased only slightly as the annealing time increased to 60 min. The AFCNO thin film had the similar phenomenon; it had the lowest resistivity of $18 \mu\Omega\text{-cm}$ after annealing at 800°C for 30 min.

Both of the TFCNO and AFCNO films had better oxidation resistance by comparing with FCNO and CFCNO films, because the titanium or aluminum atoms would diffuse to the surface and react with oxygen, thus forming a protection layer. Figure 7 shows the EPMA mapping results. Figure 7(a) shows the cross section SEM micrograph of the TFCNO film after annealing 1000°C for 30 min; and Figures 7(b)–7(f) are the corresponding mapping of Ti, O, Fe, Co, and Ni elements. The mapping of Ti and O elements indicates a titanium-oxide rich layer on the surface of the TFCNO

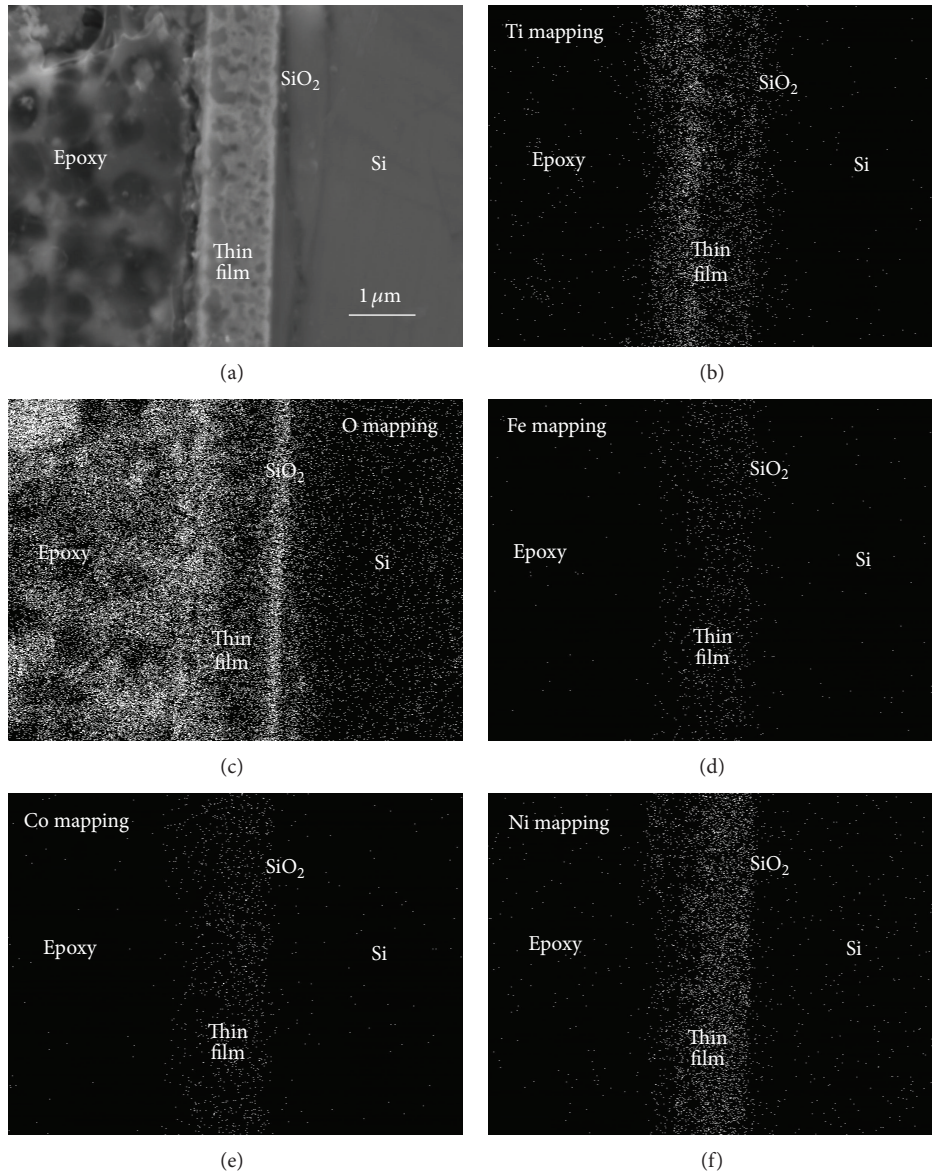


FIGURE 7: EPMA analyzed result. (a) The cross section SEM micrograph of the TFCNO thin film after annealing at 1000°C for 30 min and the corresponding element mapping of (b) Ti; (c) O; (d) Fe; (e) Co; and (f) Ni.

film. This phenomenon was described in our previous study [1]. During the first period of annealing, the tendency of Ti atoms to migrate significantly to the surface layer of the thin film and to form a Ti-rich oxide during annealing is clarified by comparing the Ti, Fe, Co, and Ni contents only based on metal elements. Therefore, the surface layer of TFCNO films was mostly Ti-rich oxides after annealing in a vacuum furnace for 30 min. The other three elements diffused to the surface layer and reacted with oxygen after annealing for over 30 min, and the resistivity thereby increased. The resistivity of the TFCNO film kept around 300 $\mu\Omega$ -cm when annealing time increased to 8 hours. This was also contributed to the addition of titanium. Titanium element thus increased the oxidation resistance of the TFCNO film. Aluminum has the similar activity with titanium [14]. Therefore, the AFCNO

film behaved similarly to the TFCNO film. The AFCNO film possessed the lowest resistivity of 18 $\mu\Omega$ -cm among these films after annealing at 800°C for 30 min; and its resistivity kept around 110 $\mu\Omega$ -cm when annealing time increased to 8 hours.

4. Conclusions

We used the equimolar concept to produce high-entropy FeCoNiO_x, CrFeCoNiO_x, AlFeCoNiO_x, and TiFeCoNiO_x oxide films and studied their resistivity after annealing at different temperatures for different periods. After optimum annealing treatment, the lowest resistivity of the FeCoNiO_x, CrFeCoNiO_x, AlFeCoNiO_x, and TiFeCoNiO_x film was 22, 42, 18, and 35 $\mu\Omega$ -cm, respectively. The room-temperature

resistivity is close to that of most of the metallic alloys. The results indicated the addition of chromium had no benefit in these alloy systems. Addition of titanium or aluminum could increase their oxidation resistance, and their resistivity kept at lower values after annealing at high temperatures for long periods.

Conflict of Interests

The authors declare that there is no conflict of interests regarding the publication of this paper.

Acknowledgment

The authors would like to thank the National Science Council, Taiwan, for financially supporting part of this research under Contract no. NSC100-2221-E-034-009.

References

- [1] Y. C. Yang, C. H. Tsau, and J. W. Yeh, "TiFeCoNi oxide thin film—a new composition with extremely low electrical resistivity at room temperature," *Scripta Materialia*, vol. 64, no. 2, pp. 173–176, 2011.
- [2] C. H. Tsau, Y. C. Yang, C. C. Lee, L. Y. Wu, and H. J. Huang, "The low electrical resistivity of the high-entropy alloy oxide thin films," *Procedia Engineering*, vol. 36, pp. 246–252, 2012.
- [3] J. Wulff, *Structure and Properties of Materials*, vol. 4, John Wiley & Sons, New York, NY, USA, 1971.
- [4] W. D. Callister Jr., *Fundamentals of Materials Science and Engineering*, John Wiley & Sons, New York, NY, USA, 2nd edition, 2005.
- [5] W. F. Smith, *Foundations of Materials Science and Engineering*, McGraw-Hill, New York, NY, USA, 3rd edition, 2004.
- [6] P.-K. Huang, J.-W. Yeh, T.-T. Shun, and S.-K. Chen, "Multi-principal-element alloys with improved oxidation and wear resistance for thermal spray coating," *Advanced Engineering Materials*, vol. 6, no. 12, pp. 74–78, 2004.
- [7] J.-W. Yeh, S.-K. Chen, S.-J. Lin et al., "Nanostructured high-entropy alloys with multiple principal elements: novel alloy design concepts and outcomes," *Advanced Engineering Materials*, vol. 6, no. 5, pp. 299–303, 2004.
- [8] J. W. Yeh, S. K. Chen, J. Y. Gan et al., "Formation of simple crystal structures in Cu-Co-Ni-Cr-Al-Fe-Ti-V alloys with multiprincipal metallic elements," *Metallurgical and Materials Transactions A*, vol. 35, pp. 2533–2536, 2004.
- [9] B. Cantor, I. T. H. Chang, P. Knight, and A. J. B. Vincent, "Microstructural development in equiatomic multicomponent alloys," *Materials Science and Engineering A*, vol. 375–377, no. 1-2, pp. 213–218, 2004.
- [10] C.-J. Tong, S.-K. Chen, J.-W. Yeh et al., "Microstructure characterization of Al_x CoCrCuFeNi high-entropy alloy system with multiprincipal elements," *Metallurgical and Materials Transactions A*, vol. 36, no. 4, pp. 881–893, 2005.
- [11] B. Gludovatz, A. Hohenwarter, D. Catoor, E. H. Chang, E. P. George, and R. O. Ritchie, "A fracture-resistant high-entropy alloy for cryogenic applications," *Science*, vol. 345, no. 6201, pp. 1153–1158, 2014.
- [12] Y. Zhang, T. T. Zuo, Z. Tang et al., "Microstructures and properties of high-entropy alloys," *Progress in Materials Science*, vol. 61, pp. 1–93, 2014.
- [13] C.-H. Tsau, "Phase transformation and mechanical behavior of TiFeCoNi alloy during annealing," *Materials Science and Engineering: A*, vol. 501, no. 1-2, pp. 81–86, 2009.
- [14] Z. Tang, M. C. Gao, H. Diao et al., "Aluminum alloying effects on lattice types, microstructures, and mechanical behavior of high-entropy alloys systems," *JOM*, vol. 65, no. 12, pp. 1848–1858, 2013.
- [15] T. S. Donovan and K. Heinemann, "High-resolution electron microscope observation of voids in amorphous Ge," *Physical Review Letters*, vol. 27, no. 26, pp. 1794–1796, 1971.
- [16] S. Tsukimoto, M. Moriyama, and M. Murakami, "Microstructure of amorphous tantalum nitride thin films," *Thin Solid Films*, vol. 460, no. 1-2, pp. 222–226, 2004.
- [17] S. Guo, C. Ng, Z. Wang, and C. T. Liu, "Solid solutioning in equiatomic alloys: limit set by topological instability," *Journal of Alloys and Compounds*, vol. 583, pp. 410–413, 2014.
- [18] Z. Wang, S. Guo, and C. T. Liu, "Phase selection in high-entropy alloys: from nonequilibrium to equilibrium," *JOM*, vol. 66, no. 10, pp. 1966–1972, 2014.

Research Article

Torsion Dependence of Domain Transition and MI Effect of Melt-Extracted $\text{Co}_{68.15}\text{Fe}_{4.35}\text{Si}_{12.25}\text{B}_{13.25}\text{Nb}_1\text{Cu}_1$ Microwires

Dawei Xing,¹ Dongming Chen,¹ Fang Liu,¹ Jingshun Liu,² Hongxian Shen,¹ Zhiliang Ning,¹ Fuyang Cao,¹ and Jianfei Sun¹

¹School of Materials Science and Engineering, Harbin Institute of Technology, No. 92 West Dazhi Street, Harbin 150001, China

²School of Materials Science and Engineering, Inner Mongolia University of Technology, No. 49 Aimin Street, Hohhot 010051, China

Correspondence should be addressed to Jianfei Sun; jfsun.hit@263.net

Received 16 October 2014; Revised 19 January 2015; Accepted 28 January 2015

Academic Editor: You Song

Copyright © 2015 Dawei Xing et al. This is an open access article distributed under the Creative Commons Attribution License, which permits unrestricted use, distribution, and reproduction in any medium, provided the original work is properly cited.

We present the torsional stress induced magnetoimpedance (MI) effect and surface domain structure evolution of magnetostrictive melt-extracted $\text{Co}_{68.15}\text{Fe}_{4.35}\text{Si}_{12.25}\text{B}_{13.25}\text{Nb}_1\text{Cu}_1$ microwires. Experimental results indicate that the surface domain structures observed by magnetic force microscope (MFM) transform from the weak circumferential domain of as-cast state to the helical domain under large torsional strain of 81.6 (2π rad/m). Domain wall movement distorts at torsional strain $\xi = 20.4$ (2π rad/m) and forms a helical anisotropy with an angle of around 30° versus axial direction of wire. At 15 MHz, the maximum of GMI ratio $\Delta Z/Z(\%)$ increases to 194.4% at $\xi = 20.4$ (2π rad/m) from 116.3% of the as-cast state and then decreases to 134.9% at $\xi = 102.0$ (2π rad/m). The torsion magnetoimpedance (TMI) ratio $(\Delta Z/Z)_\xi(\%)$ is up to 290%. Based on this large torsional strain and high MI ratio, the microwire can be as an referred candidate for high-performance TMI sensor application.

1. Introduction

The ferromagnetic microwires have been recognized as possessing much more promising magnetic sensing materials, especially for giant magnetoimpedance (GMI) effect, which has attracted considerable interest not only from the basically theoretical viewpoint but also from its wide technical applicability [1–4]. As well known, the near-zero magnetostrictive wires with soft magnetic properties have high MI ratios [1, 5]. As one method of the amorphous microwire fabrication technologies, different from glass-coated spinning and in-rotating water quenching techniques, the melt-extraction technique consists of the following: (i) it has the largest solidification or cooling rate, which enables the wires to possess an excellent soft magnetic property; (ii) the melt-extracted wires without glass covering are more suitable for electronic package and GMI sensor applications; (iii) the parameters (i.e., linear velocity of wheel, feed rate of the molten, etc.) of melt-extraction can be conveniently controlled to produce wires with uniform diameter and roundness [6, 7]. In another

perspective, near-zero magnetostrictive amorphous wires, with low resistivity ρ , high magnetic permeability μ_ϕ , high saturation magnetization M_s , and small ferromagnetic resonance (FR) in the high-frequency range, possess outstanding GMI performance. Based on this principle, the element B in CoFeSiB alloy is substituted for Nb and Cu with low resistivity materials and a small amount of atomic percentage 1% and 1%, respectively.

In the meantime, in the intermediate frequency range (100 kHz~20 MHz), GMI originates mainly from the variation of the skin depth owing to the strong changes of the effective magnetic permeability resulting in both domain wall motion and magnetization rotation; namely, it can be denoted by $\mu_\phi = \mu_{\text{wall}} + \mu_{\text{rot}}$ [1, 8]. The role of μ_{rot} gives rise to the helical anisotropy change. In order to understand deeply the role of the helical anisotropy to the surface domain and GMI performance of the near-zero magnetostrictive melt-extracted Co-based amorphous microwires, the imposed torsional strain on the microwires is necessary to observe the domain structure by magnetic force microscope (MFM)

and modify the domain transition for MI and torsion magnetoimpedance (TMI) sensor application.

Up to now, much works have previously reported the influence of torsion on MI effect for Co-based and Fe-based glass-coated or in-rotating water amorphous wires [9–13]. Betancourt and Valenzuel found the μ_ϕ an asymmetric behavior dependent on the direction of the applied torsion strain of in-rotating water ($\text{Co}_{94}\text{Fe}_6$)_{72.5}B₁₅Si_{12.5} wires [9]. Garcia et al. studied the magnetoimpedance response under tensile and torsional stress of Fe₇₆B₁₃Si₁₁ glass-coated amorphous microwires and induced a helical magnetic anisotropy that modifies the magnetic domain structure and the magnetic response of the sample applied torsion stresses [10]. Popov et al. proposed the “enhanced core-shell” model of vanishing-magnetostrictive glass-coated Co-rich microwires to resolve the physical origin of the low-field hysteresis and the dependence of induced anisotropy field on the applied tensile and/or torsional stress [11]. However, only a few researchers resorted to the surface domain structure (SDM) of twisted microwire to explore the detailed information of the modified domain and the helical anisotropy.

As well known, the core-shell magnetic structures of nearly zero magnetostrictive melt-extracted Co-based amorphous wires consist of a cylindrical inner core domain oriented axially and the outer shell domain for circumferential magnetization, while the exchange energy tilts it towards a helical orientation [14]. Generally, GMI effect is very sensitive to the magnetic structure and the local anisotropies of soft magnetic materials. It can be additionally served as a powerful tool to explore the important information of the magnetic structure and local anisotropies. Moreover, the domain structure and anisotropy field of the magnetic materials can be derived from analyzing the corresponding changes of GMI property of samples subjected to stress applied. The modification of GMI response is the consequence of the competition between the helical anisotropy introduced by the applied torsional stress and the internal anisotropies. Therefore, torsional stresses were found to modify the magnetization cycle of the wire [15], Young's modulus [16] and MI response [11], and so forth.

The aim of this work is conducted to study the static surface magnetic domain structure, MI effect of a nearly zero magnetostrictive melt-extracted Co-rich amorphous microwire dependence on applied extremely huge torsional strain and to obtain large MI value by modulating the magnetic structure and local anisotropies of soft magnetic microwires for potentially exploring the torsion MI sensors.

2. Experimental

We have prepared softly magnetic amorphous microwires of $\text{Co}_{68.15}\text{Fe}_{4.35}\text{Si}_{12.25}\text{B}_{13.25}\text{Nb}_1\text{Cu}_1$ with diameter of 35 μm by a modified melt-extraction technique [6]. Impedance measurement is carried out at the intermediate frequency range of 100 kHz~15 MHz by using Agilent 4294A precision impedance analyzer. The MR, MX, and MI ratios are defined as follows, respectively:

$$\frac{\Delta R}{R} = \frac{\langle (R(H) - R(H_{\max})) \rangle}{R(H_{\max})} \times 100\%,$$

$$\frac{\Delta X}{X} = \frac{\langle (X(H) - X(H_{\max})) \rangle}{X(H_{\max})} \times 100\%,$$

$$\frac{\Delta Z}{Z} = \frac{\langle (Z(H) - Z(H_{\max})) \rangle}{Z(H_{\max})} \times 100\%.$$

(1)

The total length of each microwire is 58 mm under the application of a torsional strain ξ ranging from 0 to 102.0 (2π rad/m) with the one end fixed and the other end rotating in clockwise direction. Then, we selected the central part of 18 mm long microwire to connect to the circuit and to measure the MI effect by the driving amplitude of 20 mA with DC axial field applied by using a pair of Helmholtz coils. The external field is up to the maximum of 80 Oe. The Helmholtz coil was kept perpendicular to the earth's magnetic field direction.

The torsion magnetoimpedance (TMI) ratio, $(\Delta Z/Z)_\xi$, or the relative change of the maximum magnetoimpedance with the torsion is expressed as follows:

$$\left(\frac{\Delta Z}{Z} \right)_\xi = \frac{\langle (Z_{\max}(\xi) - Z_{\max}(\xi_{\max})) \rangle}{Z_{\max}(\xi_{\max})} \times 100\%, \quad (2)$$

where $\xi_{\max} = 102.0$ (2π rad/m) and the external field H is 0 Oe.

Domain observation of microwire is conducted by a Nanoscope III multimode atomic force microscope from Digital Instruments. The micro-etched silicon probe tip is to collect related information by using a combination of tapping and lift mode. During lift mode, the magnetic data were collected and displayed.

3. Results and Discussion

It has been known that the changes of both resistance R and reactance X depending on μ_ϕ and external field H will alter the impedance Z and therefore are contributed to GMI behavior [1]. Based on the expression of the impedance Z of cylindrical magnetic conductor, $Z = R_{dc}kaJ_0(ka)/2J_1(ka)$ with $k = (1 + i)/\delta_m$ is expressed in terms of first order Bessel functions J_0 , J_1 and the material parameters: the skin depth δ_m , the radius a , and the dc resistance R_{dc} of the conductor. The skin depth δ_m , $\delta_m = (\rho/\pi\mu_\phi f)^{1/2}$, where ρ is the resistivity of the conductor and f is the current frequency, and the μ_ϕ is circumferential permeability. The resistance R and reactance X can be depicted as: $R = \rho l/2\pi(a - \delta_m)\delta_m$; $X = 0.175\mu_0 l f \langle \mu_\phi \rangle / \omega$, where μ_0 and μ_ϕ are the vacuum permeability and the average relative circumferential permeability, respectively [1].

Figure 1 shows the zero-field frequency dependence of resistance R (a), reactance X (b), and impedance Z (c) of microwires with torsion strain from as-cast to 102.0 (2π rad/m). An obvious monotonic increase in the resistance R (as shown in Figure 1(a)), inductive reactance X (Figure 1(b)), and impedance Z (Figure 1(c)) is observed with the frequency range of 100 kHz~15 MHz for the skin effect. And the maximum of each of R , X , and Z values is 477.7 Ω , 297.1 Ω , and 562.5 Ω , respectively, as the torsional strain increased to 20.4 (2π rad/m). Continued to increase

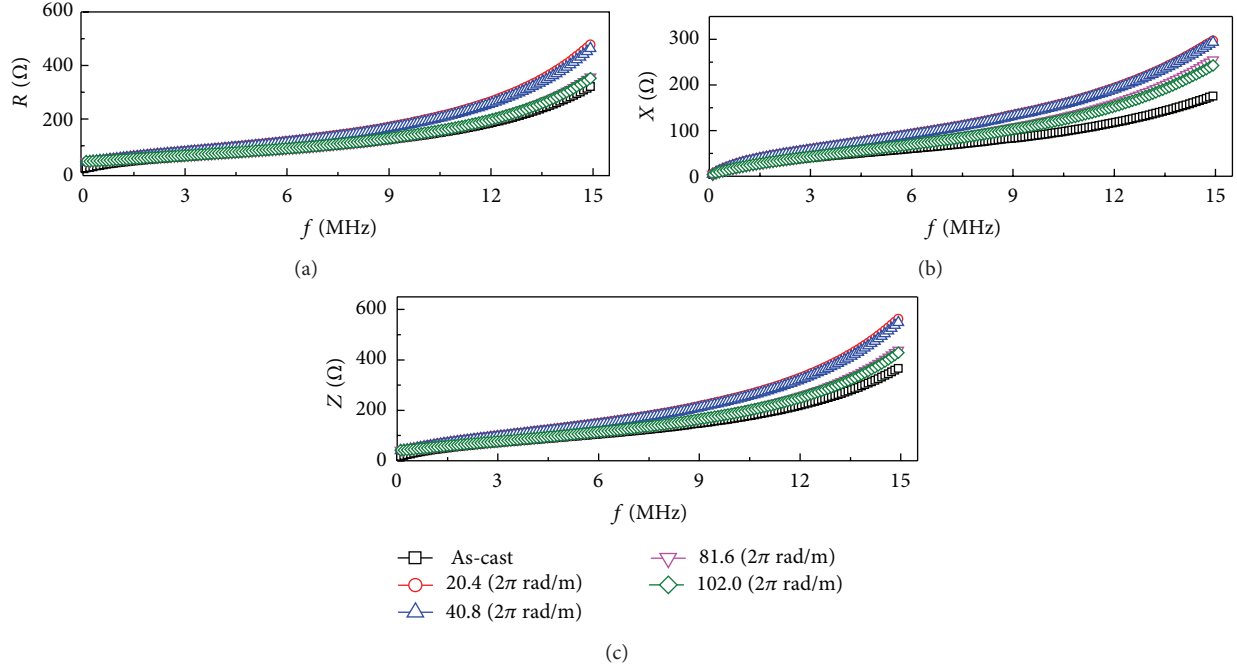


FIGURE 1: Frequency dependence of (a) resistance, (b) inductive reactance, and (c) impedance of microwires with different torsion stresses.

the torsion strain up to $40.8\sim 102.0$ (2π rad/m), all the values of R , X , and Z curves decrease. Additionally, the curves of (R , X , and Z) at torsional strain of 20.4 (2π rad/m) have a very small difference with curves of 40.8 (2π rad/m). Also a similar behavior displays between curves of 81.2 (2π rad/m) torsional strain with 102.0 (2π rad/m) torsional strain. At the intermediate frequency regime, skin effect is dominant and the impedance is proportional to the square root of frequency and circumferential permeability; namely, $Z \propto (\omega\mu_\phi)^{1/2}$. The influence of torsion stress on the microwire will improve the circular permeability μ_ϕ at a certain extent. Therefore, the corresponding values of R , X , and Z for the torsional microwires all increase with the frequency.

Figure 2 reveals the magnetic field dependence of the magnetoresistance $\Delta R/R\%$ (Figure 2(a)), magnetoinductive reactance $\Delta X/X\%$ (Figure 2(b)), and magnetoimpedance $\Delta Z/Z\%$ (Figure 2(c)) ratios at $f = 15$ MHz for applied torsion ξ from 0 to 102.0 (2π rad/m). In comparison with the behavior of $\Delta R/R\%$ and $\Delta Z/Z\%$, the curves of $\Delta X/X\%$ (Figure 2(b)) appear to the peaks with positions from 0.4 Oe to 0.7 Oe for torsion strain from 20.4 (2π rad/m) to 102.0 (2π rad/m). This torsion stress can be considered to change greatly the permeability. In addition, this response of the microwire is attributed to two magnetization processes: spin rotation and bulging of pinned domain walls. As shown in Figure 2(c), the curves of $\Delta Z/Z\%$ also exhibit the increasing trend at $\xi = 20.4$ (2π rad/m) and then decrease with the ξ to 102.0 (2π rad/m). The magnified plot of the peak value of $\Delta Z/Z\%$ inserted in the Figure 2(c) displays the ratio of $(\Delta Z/Z)_{\max}\%$ from 116.2% at as-cast to 194.4% at $\xi = 20.4$ (2π rad/m) for $f = 15$ MHz. This enhanced improvement can be attributed to the releasing

residual stress and the modified surface domain structure, as shown in Figure 3(b).

The behavior of GMI profiles is well resolved by considering the domain model with periodically circular domains [17]. Large μ_ϕ is contributed to the high GMI ratio and well-defined circumferential domain structure [18]. Therefore, we can improve the circumferential permeability μ_ϕ and impedance Z by modulating the surface domain structure.

Accordingly, the surface morphology, domain structure obtained by MFM, and the schematic plot of microwire are presented for untwisted and under torsional strain state in Figure 3. The surface domain structure of the microwire of as-cast state is showed in Figure 3(a). The ill-defined circumferential domain configuration is exhibited with the average domain width of about 1.0 μm . The weak and uneven circumferential domain on the whole surface result from the microwire preparation process and the weak circular magnetic anisotropy. The residual stress and even heterogeneous microstructure of microwire all are not conducive to the formation of circumferential domain. So the corresponding the ratio of $(\Delta Z/Z)_{\max}$ is only 116.2% . In order to induce helical anisotropy and further to influence the magneto-impedance response, each microwire was submitted to a homogenous torsional stress to form even domain structure. The modification of domain structure with increasingly applied torsion is obtained in Figures 3(b), 3(c), and 3(d). For $\xi = 20.4$ (2π rad/m), the surface morphology of the microwire appears distortion for the surface roughness of dozens of nanometers. Moreover, the domain structure was observed clearly with torsion stress applied to the wire in middle part of Figure 3(b).

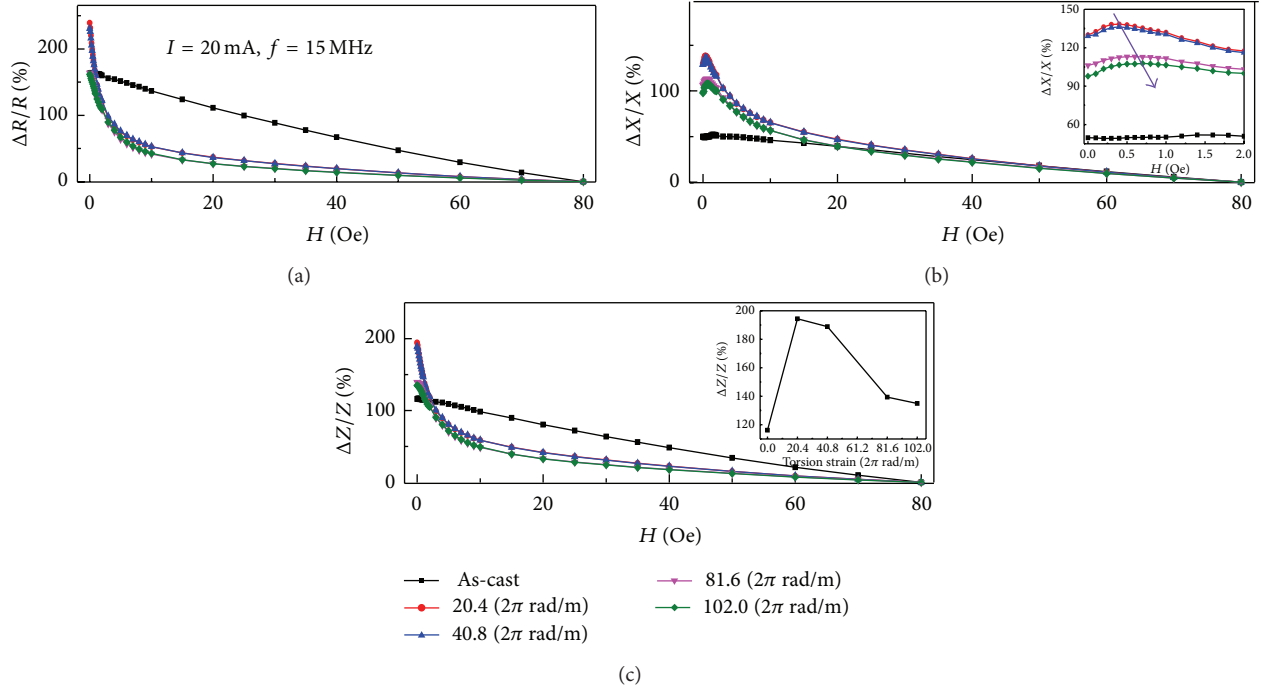


FIGURE 2: Magnetic field dependence of the magnetoresistance ($\Delta R/R$), magnetoreactance ($\Delta X/X$), and magnetoimpedance ($\Delta Z/Z$) ratios at $f = 15$ MHz for selectively applied torsion. And insets of the magnified peak positions of $\Delta X/X$ in (b) and of the maximum values of $\Delta Z/Z$ dependence to torsion strain in (c).

Different from the weak circumferential domain of as-cast state, the surface domain with the torsional state $\xi = 20.4$ (2π rad/m) turns to form the zigzag domain, which is derived from the helical anisotropy. The relatively large GMI ratio on this stage is contributed from the enhanced circumferential anisotropy generated by circular component of torsion stress. Additionally, the circumferential component of helical anisotropy induced by applied the torsional stress improves the circular anisotropy, which is benefit for circumferential permeability μ_ϕ , further for GMI ratios improvement. Consequently, the average domain width increases to $1.1 \mu\text{m}$ at $\xi = 20.4$ (2π rad/m). For this circumstance, the circumferential domain turns to zigzag domain under the torsional strain, at which behavior is different from the consistency deflection for positive magnetostrictive Fe-based wires [19]. As the applied torsion increases to 61.2 (2π rad/m) in Figure 3(c), the uneven domain is changed into more clear domain and smooth domain wall with average width about $0.9 \mu\text{m}$ and tilt angle θ up to about 67° . Further to apply the torsional strain to 81.6 (2π rad/m), the uniform helical domain is obtained with domain wall angle $\theta \approx 30^\circ$. Based on the extreme torsion applied, GMI profile exhibits the maximum of 139.4% at $\xi = 81.6$ (2π rad/m). The slight difference between GMI ratios of $\xi = 81.6$ (2π rad/m) and $\xi = 102.0$ (2π rad/m) indicates the surface domain in each case is very similar. Momently, a uniform helical domain is therefore formed with smaller domain wall angle of $\theta \approx 30^\circ$, at which performance manifests the homogeneous and larger helical anisotropy. Additionally, an interesting result of

Co-based melt-extracted microwires with large torsion strain performance of $\xi = 102.0$ (2π rad/m) will be as the ideal candidate potential materials for high-performance torsion TMI sensor [20].

To sum up, the torsional strain ξ dependence of torsional impedance profile $(\Delta Z/Z)_\xi$ and domain wall angle θ is illustrated in Figure 4. As observed, the $(\Delta Z/Z)_\xi$ ratios decrease with the increasing torsional strain ξ . The maximum ratio $(\Delta Z/Z)_\xi$ is up to 290% . Combining with the domain transformation applied different torsional strain (Figure 3), the domain wall movement is neither ideally towards longitudinal nor uniformly with a helical component along the axial direction. The domain wall distortion firstly is perpendicular to the axial direction (Figure 3(b)) and then tilts to transverse direction with a small angle (Figure 3(c)) and forms a helical magnetic anisotropy making an angle about 30° with the longitudinal direction (Figure 3(d)). So the large torsional strain is up to 102.0 (2π rad/m) as the candidate for torsion magnetoimpedance (TSI) application.

4. Summary

In conclusion, we have systematically investigated the surface domain transition and MI effect of Co-based melt-extracted microwires at different torsional strain. Firstly, the Co-based microwire is revealed to achieve the huge torsion strain behavior of $\xi = 102.0$ (2π rad/m). We also observed an increased MI ratio as a result of modification of the helical magnetic anisotropy. Accordingly, the domain transformation under torsion stress corresponding to the GMI profile

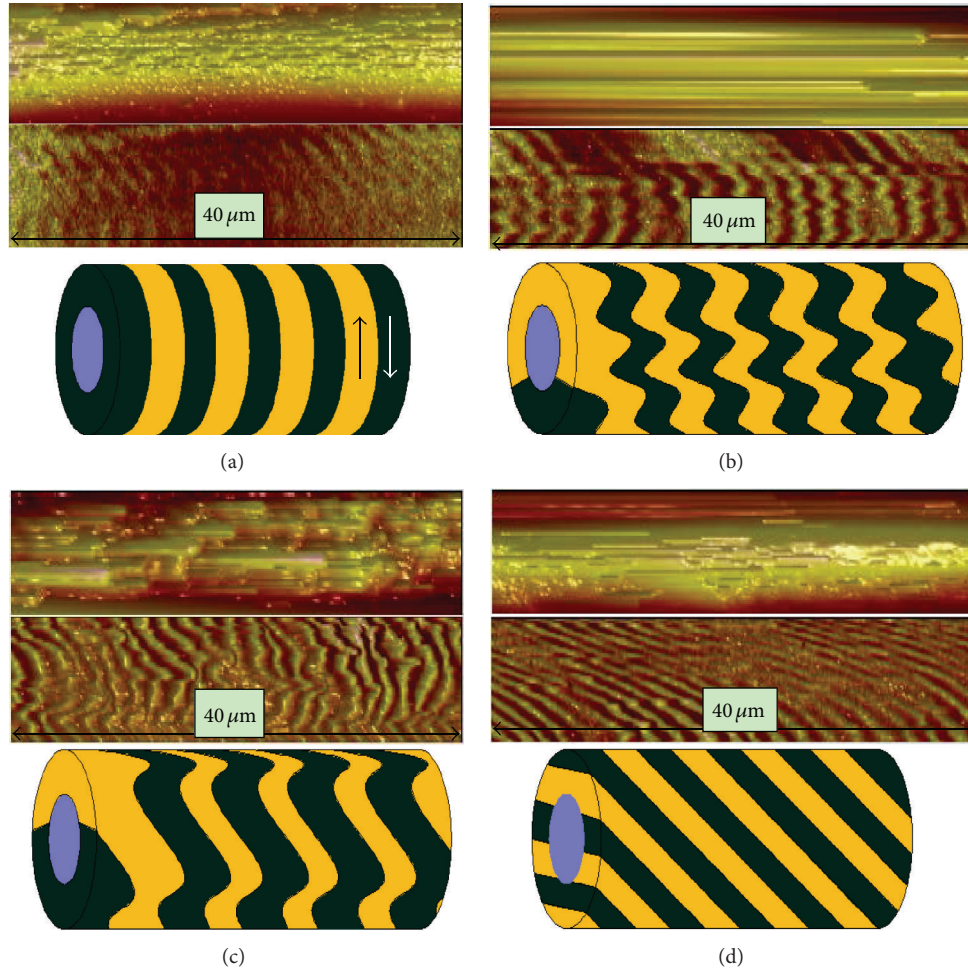


FIGURE 3: Surface domain structures transition and corresponding schematic diagrams of $\text{Co}_{68.15}\text{Fe}_{4.35}\text{Si}_{12.25}\text{B}_{13.25}\text{Nb}_1\text{Cu}_1$ amorphous wires: (a) as-prepared and under different values of the applied torsion in the clockwise sense: (b) $\xi = 20.4 (2\pi \text{ rad/m})$, (c) $\xi = 61.2 (2\pi \text{ rad/m})$, and (d) $\xi = 81.6 (2\pi \text{ rad/m})$.

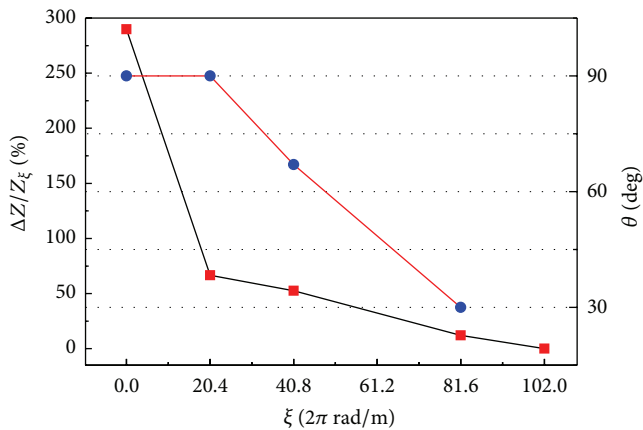


FIGURE 4: Torsional strain ξ dependence of the maximum MI ratios and domain wall angle θ .

exhibits the heterogeneous transition. And the obtained results on large torsion magnetoimpedance ratio $(\Delta Z/Z)_\xi$ to

290% can be suitable for further development of the high-performance torque TSI sensors.

Conflict of Interests

The authors declare that there is no conflict of interests regarding the publication of this paper.

Acknowledgments

Dawei Xing acknowledges the financial support provided by the Natural Science Foundation of China (NSFC) under Grant no. 51371067. Jingshun Liu acknowledges the supports from NSFC with Grant no. 51401111, Natural Science Foundation of Inner Mongolia Autonomous Region of China under Grant no. 2014BS0503, and Scientific Research Foundation of the Higher Education Institutions (SRFHEI) of Inner Mongolia Autonomous Region of China under Grant no. NJZY14062.

References

- [1] M. H. Phan and H. X. Peng, "Giant magnetoimpedance materials: fundamentals and applications," *Progress in Materials Science*, vol. 53, no. 2, pp. 323–420, 2008.
- [2] L. V. Panina and K. Mohri, "Magneto-impedance effect in amorphous wires," *Applied Physics Letters*, vol. 65, no. 9, pp. 1189–1191, 1994.
- [3] F. X. Qin and H. X. Peng, "Ferromagnetic microwires enabled multifunctional composite materials," *Progress in Materials Science*, vol. 58, no. 2, pp. 183–259, 2013.
- [4] A. Zhukov and V. Zhukova, *Magnetic Properties and Applications of Ferromagnetic Microwires with Amorphous and Nanocrystalline Structure*, Nova Science Publishers, New York, NY, USA, 2009.
- [5] M. Knobel and K. R. Pirota, "Giant magnetoimpedance: concepts and recent progress," *Journal of Magnetism and Magnetic Materials*, vol. 242–245, pp. 33–40, 2002.
- [6] H. Wang, D. W. Xing, X. D. Wang, and J. F. Sun, "Fabrication and characterization of melt-extracted co-based amorphous wires," *Metallurgical and Materials Transactions A*, vol. 42, no. 4, pp. 1103–1108, 2011.
- [7] J. Liu, F. Qin, D. Chen et al., "Combined current-modulation annealing induced enhancement of giant magnetoimpedance effect of co-rich amorphous microwires," *Journal of Applied Physics*, vol. 115, no. 17, Article ID 17A326, 2014.
- [8] L. V. Panina, K. Mohri, T. Uchiyama, M. Noda, and K. Bushida, "Giant magneto-impedance in Co-rich amorphous wires and films," *IEEE Transactions on Magnetics*, vol. 31, no. 2, pp. 1249–1260, 1995.
- [9] I. Betancourt and R. Valenzuel, "Effect of helical-induced anisotropy on the magnetoinductance response of Co-based amorphous wires," *Applied Physics Letters*, vol. 83, p. 2022, 2003.
- [10] C. Garcia, A. Chizhik, A. Zhukov et al., "Influence of torsion and tensile stress on magnetoimpedance effect in Fe-rich amorphous microwires at high frequencies," *Journal of Magnetism and Magnetic Materials*, vol. 316, no. 2, pp. e896–e899, 2007.
- [11] V. V. Popov, V. N. Berzhansky, H. V. Gomonay, and F. X. Qin, "Stress-induced magnetic hysteresis in amorphous microwires probed by microwave giant magnetoimpedance measurements," *Journal of Applied Physics*, vol. 113, no. 17, Article ID 17A326, 2013.
- [12] Y. F. Li, M. Vázquez, and D. X. Chen, "Torsion-dependent magnetoimpedance in FeCuNbSiB nanocrystalline wires with vanishing or transverse anisotropy," *Journal of Applied Physics*, vol. 93, no. 12, pp. 9839–9844, 2003.
- [13] J. M. Blanco, A. Zhukov, A. P. Chen, A. F. Cobeno, A. Chizhik, and J. Gonzalez, "Asymmetric torsion giant impedance in nearly-zero magnetostrictive amorphous wires with induced helical anisotropy," *Journal of Physics D: Applied Physics*, vol. 34, no. 6, pp. L31–L34, 2001.
- [14] P. Ciureanu, I. Khalil, L. G. C. Melo, P. Rudkowski, and A. Yelon, "Stress-induced asymmetric magneto-impedance in melt-extracted Co-rich amorphous wires," *Journal of Magnetism and Magnetic Materials*, vol. 249, no. 1-2, pp. 305–309, 2002.
- [15] L. P. Shen, T. Uchiyama, K. Mohri, E. Kita, and K. Bushida, "Sensitive stress-impedance micro sensor using amorphous magnetostrictive wire," *IEEE Transactions on Magnetics*, vol. 33, no. 5, pp. 3355–3357, 1997.
- [16] S. Atalay, P. T. Squire, and P. Rudkowski, "Magnetic and magnetoelastic properties of Fe-Si-B metallic fibers," *IEEE Transactions on Magnetics*, vol. 32, no. 5, pp. 4875–4877, 1996.
- [17] D. X. Chen, J. Muñoz, A. Hernando, and M. Vázquez, "Magnetoimpedance of metallic ferromagnetic wires," *Physical Review B*, vol. 57, no. 17, pp. 10699–10704, 1998.
- [18] D.-M. Chen, D.-W. Xing, F.-X. Qin et al., "Correlation of magnetic domains, microstructure and GMI effect of Joule-annealed melt-extracted $\text{Co}_{68.15}\text{Fe}_{4.35}\text{Si}_{12.25}\text{B}_{13.75}\text{Nb}_1\text{Cu}_{0.5}$ microwires for double functional sensors," *Physica Status Solid A*, vol. 210, no. 11, pp. 2515–2520, 2013.
- [19] B. Hernando, M. L. Sánchez, V. M. Prida et al., "Magnetic domain structure of amorphous $\text{Fe}_{73.5}\text{Si}_{13.5}\text{B}_9\text{Nb}_3\text{Cu}_1$ wires under torsional stress," *Journal of Applied Physics*, vol. 103, no. 7, Article ID 07E716, 2008.
- [20] M. Tejedory, B. Hernandoy, M. L. Sánchez, V. M. Priday, and M. Vázquez, "The torsional dependence of the magnetoimpedance effect in current-annealed Co-rich amorphous wires," *Journal of Physics D: Applied Physics*, vol. 31, no. 23, pp. 3331–3336, 1998.

Research Article

The Effect of Stoichiometry on Hydrogen Embrittlement of Ordered Ni₃Fe Intermetallics

Y. X. Chen,^{1,2} Tao Chen,² and Haiyan Qian²

¹Laboratory for Microstructure, Shanghai University, Shanghai 200072, China

²Institute of Materials Science, Shanghai University, Shanghai 200072, China

Correspondence should be addressed to Y. X. Chen; yxchen@shu.edu.cn

Received 23 October 2014; Revised 14 January 2015; Accepted 16 January 2015

Academic Editor: Jianfei F. Sun

Copyright © 2015 Y. X. Chen et al. This is an open access article distributed under the Creative Commons Attribution License, which permits unrestricted use, distribution, and reproduction in any medium, provided the original work is properly cited.

The effects of Fe stoichiometry on hydrogen embrittlement and hydrogen diffusion in ordered Ni₃Fe intermetallics were investigated. The experimental results show that the ordered Ni₃Fe alloy with the normal stoichiometry has the lowest mechanical property, the highest susceptibility to hydrogen, and the highest ability of catalytic reaction. The mechanical properties, the susceptibility to hydrogen embrittlement, and the amount of adsorbed hydrogen of the ordered Ni₃Fe alloy are dependent of degree of order of the alloy. The apparent hydrogen diffusion coefficient of the ordered Ni₃Fe alloy is independent on degree of order of the alloy but depends on Fe stoichiometry. The activation energy of hydrogen diffusion decreased linearly with Fe stoichiometry for the ordered Ni₃Fe alloy.

1. Introduction

Intermetallics have the good properties of high specific strength, high temperature resistance, and excellent corrosion resistance. But there exists the environmental embrittlement at room temperature for intermetallics [1]. The environmental embrittlement of intermetallics has been proved to be a hydrogen embrittlement process. Among Fe-Ni alloys, Ni₃Fe (permalloy) is known as soft magnetic [2, 3] intermetallic compound that presents a AuCu₃ type Pm3m space group face-centered cubic (FCC) structure. Ni₃Fe phase is a solid solution not having a single component. There is a disorder-order transformation in the critical temperature T_c for Ni₃Fe alloy, which is about 500°C. There is no H₂-induced environmental embrittlement for the disordered Ni₃Fe in gaseous hydrogen; however, the H₂-induced embrittlement for the ordered alloy (L1₂ crystal structure) having the same chemical composition becomes severer [4]. The susceptibility of the ordered Ni₃Fe alloy to hydrogen embrittlement increases with increasing degree of order [5]. The mechanism of hydrogen embrittlement for Ni₃Fe alloy is that the transitional elements on the surface catalyze H₂ molecule in environment into H atom, and then atomic

hydrogen diffuses into materials, segregates at the grain boundaries, and decreases the grain-boundary cohesion [6]. This mechanism has been confirmed by the experimental results of adsorption-desorption of hydrogen on the surface of Ni₃Fe alloy [7, 8]. The effect of B suppressing the environmental embrittlement of ordered Ni₃Al alloy depends on Al stoichiometry of the alloy. It was suggested that alloy stoichiometry strongly influences grain-boundary chemistry which, in turn, affects the grain-boundary cohesion [9]. It was found that the phase composition and the grain size of Ni₃Fe alloy are independent of Fe stoichiometry, and the effect of Fe stoichiometry on the mechanical properties of the ordered alloy is larger than that of disordered alloy [10]. The apparent hydrogen diffusion coefficient decreases with increasing the boron concentration doped in the ordered Ni₃Fe alloy, and the doping boron in the Ni₃Fe alloy is effective in reducing the hydrogen diffusion at the grain boundary [11]. Therefore, Ni₃Fe alloy is an ideal alloy for studying the effect of the stoichiometry on susceptibility to hydrogen embrittlement of ordered intermetallics. The purpose of this paper is to determine the effect of stoichiometry on a mechanism of hydrogen embrittlement and hydrogen diffusion for the ordered Ni₃Fe intermetallics.

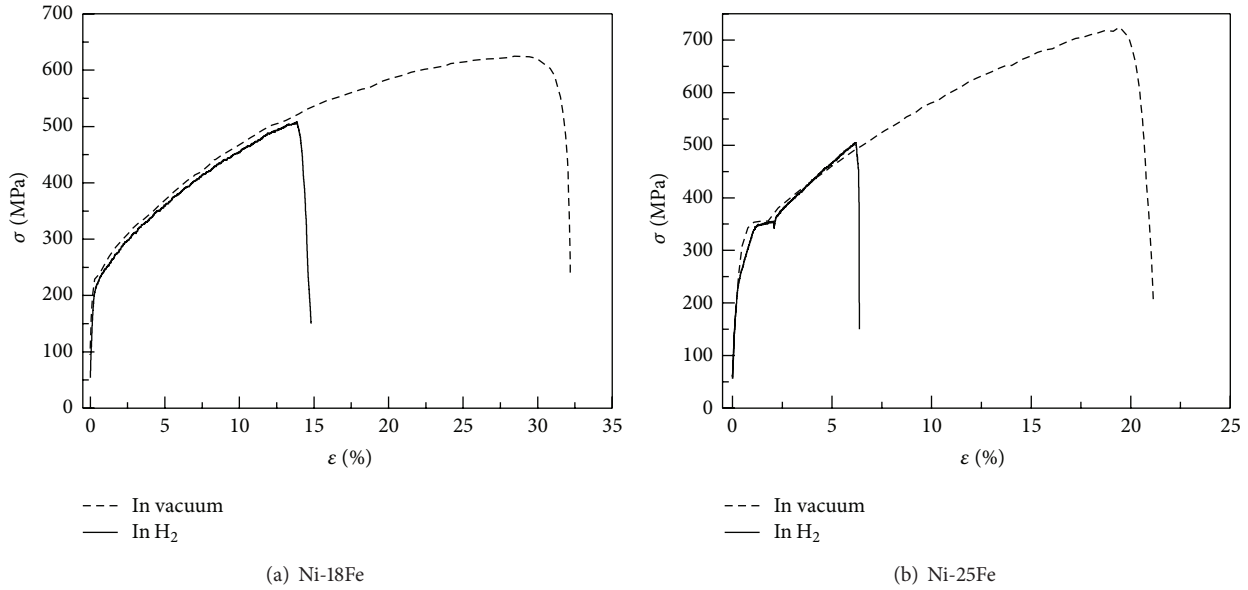


FIGURE 1: Engineering stress-strain curves for the ordered Ni_3Fe alloys with different stoichiometry when tested in vacuum and H_2 .

2. Experimental Procedure

Several Ni_3Fe alloys with different stoichiometry, Ni-18Fe, Ni-22Fe, Ni-25Fe, and Ni-28Fe, (all in at.%) were prepared by arc melting high purity of Ni and Fe. The ingots were hot rolled to sheets of 2 mm at 1050°C . Then the sheets were cold rolled to sheets of about 1 mm thickness after stress relief annealing. Tensile specimens with a gage section of $10 \times 2 \times 1$ mm were electric discharge machined from the sheets and sealed in an evacuated quartz tube. The specimens were disordered by annealing at 800°C for 2 h, and then the capsule was broken under water. For ordering treatment, some disorder treated specimens were sealed also in evacuated quartz tubes and annealed at 470°C for 200 h, followed by furnace cooling. Tensile tests were conducted on an MTS machine equipped with a vacuum chamber. For tensile testing in gaseous hydrogen, the chamber was evacuated twice to a pressure of about 2×10^{-2} Pa and backfilled with pure hydrogen gas released from hydrogen-storage materials (the purity of H_2 is about 99.999%). All tensile tests were carried out at the constant nominal strain rate of $2 \times 10^{-3} \text{ s}^{-1}$ and at room temperature. The ductility of the alloys was obtained by comparing the length of gage section before and after fracture. The fracture surface of tested specimens was examined by scanning electron microscopy (SEM). The depth of intergranular (IG) fracture on a fracture surface was also measured in situ by SEM.

The hydrogen adsorption by Ni_3Fe powder with different stoichiometry was conducted on the impulsive adsorption apparatus. The Ni_3Fe powder was made by mechanical alloying using pure Ni and Fe powders. The hydrogen adsorption experiment was performed in a flow system using a thermal conductivity detector (TCD) to monitor the variation of H_2 concentration. The hydrogen adsorption experiment was described detailedly in [7].

In order to study the effect of Fe stoichiometry on diffusion coefficient of hydrogen, the sheet specimens were cathodically precharged with hydrogen at 25°C , 35°C , or 45°C for 5 h, respectively. A charging current density of 45 mA/cm^2 was applied to the unmasked gage length area. The electrolyte was $0.5 \text{ mol/l H}_2\text{SO}_4$ solution poisoned with 50 mg/l NaAsO_2 . After charging, the specimens were quickly rinsed first in distilled water and then in acetone and alcohol, respectively. After being dried by blowing air at room temperature, the specimens were immersed in liquid nitrogen to limit the redistribution of charging hydrogen. Tensile test of the charging specimens was conducted on an MTS machine in vacuum condition at room temperature and at the nominal strain rate of $2 \times 10^{-3} \text{ s}^{-1}$. A diffusion coefficient of hydrogen of the ordered Ni_3Fe with different stoichiometry was calculated by time lag method, which was described in [11].

3. Results and Discussion

It was found that there is only single phase in the disordered Ni_3Fe alloys with different stoichiometry, which means that the stoichiometry of Ni_3Fe alloy with the studied composition does not change the phase composition of the alloy [10]. Figure 1 illustrates the engineering stress-strain curves of the ordered Ni-18Fe and Ni-25Fe alloy when tensile tested in vacuum and gaseous hydrogen. The stress-strain curves of the ordered Ni-22Fe and Ni-28Fe are similar to that of Ni-25Fe. The mechanical properties of the ordered Ni_3Fe with different stoichiometry when tested in vacuum and in H_2 are listed in Table 1. Figure 2 shows the relation curve between the maximum tensile strength (σ_{max}) and Fe stoichiometry for the ordered Ni_3Fe alloy in vacuum and H_2 . It can be seen from Figure 2 that σ_{max} increases firstly and decreases and then increases again when Fe stoichiometry changes from

TABLE 1: The mechanical properties of the ordered Ni₃Fe alloy with different stoichiometry when tested in vacuum and H₂.

Alloy	In vacuum		In H ₂		<i>I</i> _{H₂} , %
	σ_{\max} , MPa	δ , %	σ_{\max} , MPa	δ , %	
Ni-18Fe	627.7	32.5	509.3	15.6	51.9
Ni-22Fe	762.3	28.2	616.8	11.9	57.7
Ni-25Fe	725.9	23.4	505.7	6.9	70.7
Ni-28Fe	958.3	30.8	681.1	10.4	66.2

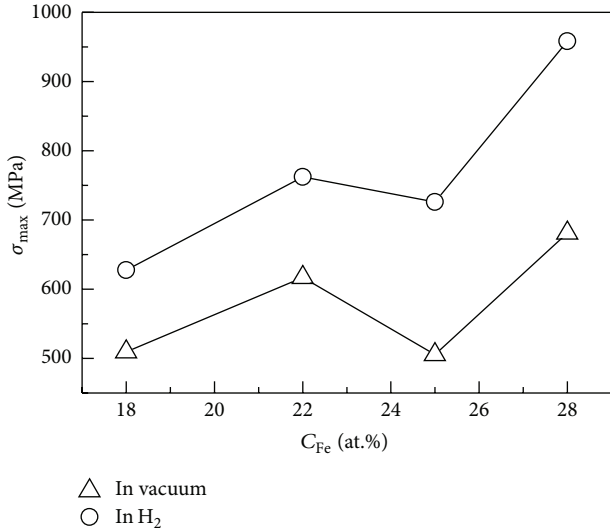


FIGURE 2: Relationship between the maximum tensile strength and Fe stoichiometry.

18 at.% to 28 at.%. The change of the stoichiometry of alloy alters contents and kinds of point defect and degree of order of the alloy, which affects the mechanical properties of the ordered Ni₃Fe alloy [10]. The change range of tensile strength of the ordered Ni₃Fe when tested in vacuum is larger than that when tested in H₂.

It can be seen from Figure 2 that σ_{\max} when tested in vacuum is all higher than that when tested in H₂ for the ordered Ni₃Fe alloy with the same stoichiometry because of the effect of hydrogen embrittlement. The effect of the hydrogen embrittlement varies with Fe stoichiometry of Ni₃Fe alloy. We define a parameter $\Delta\sigma_{\max}$ to describe the effect of the hydrogen embrittlement on σ_{\max} ; $\Delta\sigma_{\max}$ is defined as follows:

$$\Delta\sigma_{\max} = \sigma_{\max}^{\text{in H}_2} - \sigma_{\max}^{\text{in vacuum}}, \quad (1)$$

where $\sigma_{\max}^{\text{in vacuum}}$ and $\sigma_{\max}^{\text{in H}_2}$ are the maximum tensile strength of the ordered alloy when tested in vacuum and in H₂, respectively. According to the data of Figure 2, we can plot the curve of $\Delta\sigma_{\max}$ versus C_{Fe} (Figure 3). It is showed in Figure 3 that $\Delta\sigma_{\max}$ value induced by the hydrogen embrittlement decreases with the increase of Fe stoichiometry of the ordered Ni₃Fe alloy. The higher the maximum tensile strength of the ordered alloy in vacuum, the larger the effect of the hydrogen embrittlement on σ_{\max} .

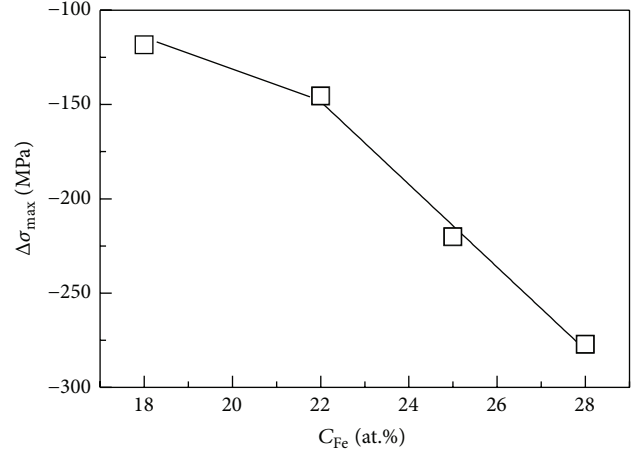
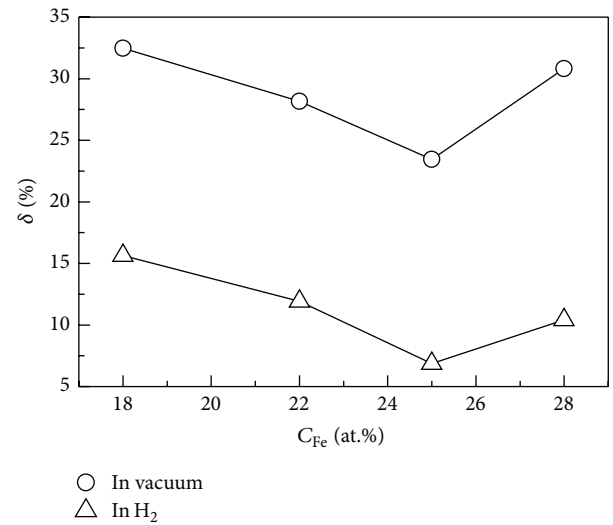
FIGURE 3: The curve of $\Delta\sigma_{\max}$ versus C_{Fe} .FIGURE 4: The change of elongation of the ordered Ni₃Fe with Fe stoichiometry when testing in vacuum and in H₂.

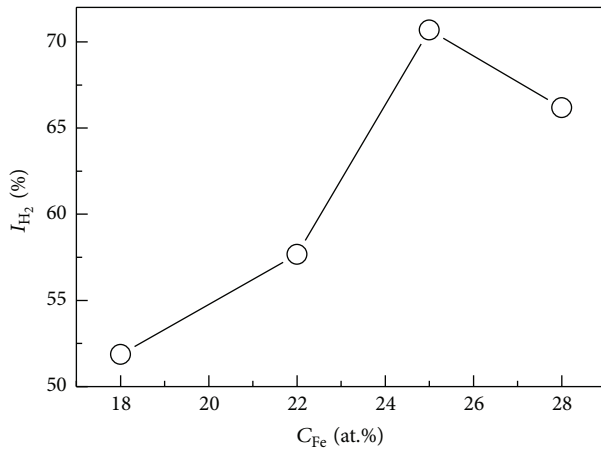
Figure 4 illustrates the changes of elongation of the ordered Ni₃Fe alloy when tested in vacuum and in H₂ with Fe stoichiometry. Different from the change of the tensile strength with Fe stoichiometry, the elongation of alloy increases linearly with increasing the extent of deviating the normal stoichiometry, and the elongation of the normal stoichiometric ordered Ni₃Fe alloy is the lowest in the studied alloy. The elongations of the alloy when tested in H₂ are all lower than that when tested in vacuum for the ordered Ni₃Fe having the same stoichiometry because of the effect of hydrogen embrittlement.

Generally, the susceptibility to hydrogen embrittlement of a material is characterized by a factor of hydrogen embrittlement (*I*_{H₂}). The factor of hydrogen embrittlement is defined as

$$I_{\text{H}_2} = \frac{\delta_{\text{vacuum}} - \delta_{\text{H}_2}}{\delta_{\text{vacuum}}} \times 100\%, \quad (2)$$

TABLE 2: The value of x and D_A of the ordered Ni₃Fe alloy with different stoichiometry precharged hydrogen at various conditions.

Alloy	25°C		35°C		45°C		Q, kJ/mol
	$x, \mu\text{m}$	$D_A, \text{cm}^2/\text{s}$	$x, \mu\text{m}$	$D_A, \text{cm}^2/\text{s}$	$x, \mu\text{m}$	$D_A, \text{cm}^2/\text{s}$	
Ni-22Fe	44.86	1.86×10^{-10}	58.15	3.13×10^{-10}	72.29	4.84×10^{-10}	37.64
Ni-25Fe	27.69	7.10×10^{-11}	34.73	1.12×10^{-10}	41.83	1.62×10^{-10}	32.54
Ni-28Fe	22.50	4.69×10^{-11}	27.03	6.77×10^{-11}	31.55	9.22×10^{-11}	26.65

FIGURE 5: The factor of hydrogen embrittlement of the ordered Ni₃Fe versus Fe stoichiometry.

where δ_{vacuum} is the elongation of the material when tensile tested in vacuum and δ_{H_2} is the elongation of the material when tensile tested in H₂.

I_{H_2} of the ordered Ni₃Fe alloy with different stoichiometry is listed also in Table 1. Figure 5 shows that I_{H_2} of the ordered Ni₃Fe alloy changes with Fe stoichiometry. It can be seen from Table 1 and Figure 5 that I_{H_2} of the ordered Ni₃Fe alloy increases firstly and then decreases with the increase of Fe stoichiometry. I_{H_2} of the ordered Ni₃Fe alloy with the normal stoichiometry is the largest in the studied alloy. This means that the susceptibility of the ordered Ni₃Fe alloy with the normal stoichiometry to hydrogen embrittlement is the largest in the ordered Ni₃Fe.

Fractographs of the ordered Ni₃Fe with different stoichiometry when tested in vacuum are showed in Figure 6. It can be seen from Figure 6 that the fracture surfaces of the ordered Ni₃Fe with different stoichiometry when tensile tested in vacuum present all 100% transgranular fracture. But examination of the fracture surface failing in gaseous H₂ reveals that the ordered Ni-18Fe and Ni-28Fe failed by a mixed transgranular-intergranular rupture as shown in Figures 7(a) and 7(c) whereas the ordered Ni-25Fe (normal stoichiometry) exhibited very brittle fracture, that is, with 100% intergranular fracture (Figure 7(b)). Thus, the observed fractographs are quite consistent with the elongation and ultimate tensile strength listed in Table 1.

The experimental results approved that the higher sensitivity to H₂-induced environmental embrittlement of the ordered Ni₃Fe in gaseous H₂ was attributed to the enhancement of the catalytic reaction on the surfaces to produce

more atomic hydrogen [7]. The effect of Fe stoichiometry on ability of catalysis has been studied by the impulsive adsorption apparatus. Figure 8 illustrates that the specific capacity of adsorbed hydrogen by the ordered Ni₃Fe powder varies with Fe stoichiometry of the alloy. It can be seen from Figure 8 that the amount of adsorbed hydrogen by the normal stoichiometric Ni₃Fe alloy is the largest in all studied Ni₃Fe powder. This means that there is an effect of the Fe stoichiometry on the ability of catalytic reaction to produce atomic hydrogen. Because of the relation between the Fe stoichiometry and degree of order in the ordered Ni₃Fe alloy [10], it is suggested that the ability of catalytic reaction of the ordered Ni₃Fe alloy depends on degree of order of the alloy.

It was found that the factor of hydrogen embrittlement of the ordered Ni₃Fe alloy increases linearly with increasing degree of order of alloy [5]. According to results of Figure 5, the ordered Ni₃Fe alloy with the normal stoichiometry should have the highest degree of order in four Ni₃Fe alloys studied in this experiment. The experimental results approved that the change of the stoichiometry of Ni₃Fe alloy altered degree of order of the alloy, which affected the mechanical properties of the ordered Ni₃Fe alloy [10]. Similarly, it is also confirmed in this paper that the Fe stoichiometry alters degree of order of the ordered Ni₃Fe, which changes the susceptibility of the ordered Ni₃Fe to hydrogen embrittlement.

The hydrogen embrittlement contains generation of the atomic hydrogen and hydrogen atom diffusion in the alloy. Thus, the diffusion of hydrogen is an important step of the hydrogen embrittlement. After precharged with hydrogen at various temperatures for 5 h, the mechanical properties of the sheet specimens of Ni-22Fe, Ni-25Fe, and Ni-28Fe were investigated by tensile test in vacuum at room temperature. The average depth of IG fracture (x) was measured in situ by SEM and a value of x is obtained by averaging twenty measurement data from both sides of each specimen after rupture. Table 2 shows x value measured for the ordered Ni₃Fe alloy with various stoichiometric ratios charging hydrogen at different temperatures. It can be seen from this table that the depth of IG fracture of the ordered Ni₃Fe alloys decreases with the increment of Fe stoichiometry at the same precharging temperature. The apparent hydrogen diffusion coefficient (D_A) of the ordered Ni₃Fe alloy may be calculated by the depth of IG fracture and the time lag method [11]. The calculated apparent hydrogen diffusion coefficient of the ordered Ni₃Fe alloy with various stoichiometries is also listed in Table 2. It can be seen from Table 2 that the change of the apparent hydrogen diffusion coefficient of the ordered Ni₃Fe alloy is consistent with change of the depth of IG fracture when changing the precharging temperature or Fe

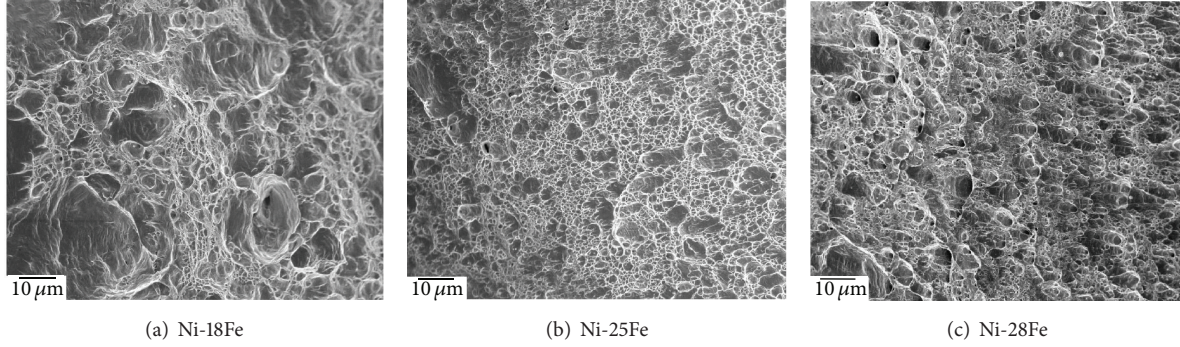


FIGURE 6: SEM fractographs of the ordered Ni₃Fe with different stoichiometry when tested in vacuum.

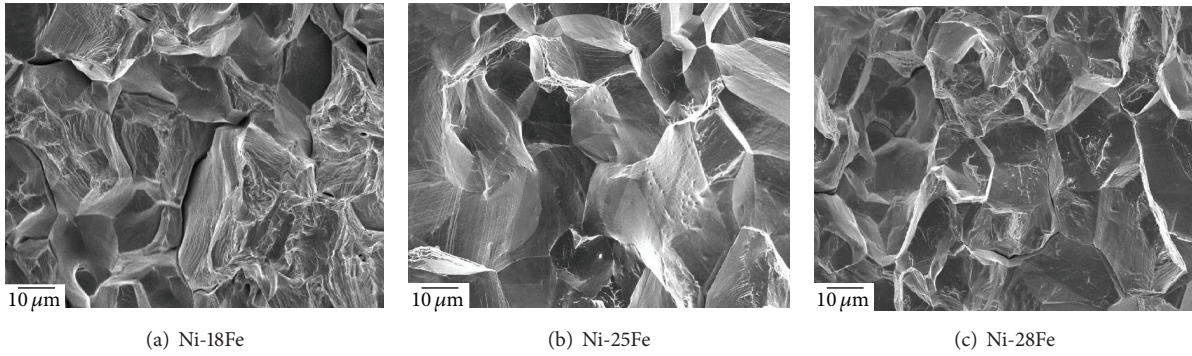


FIGURE 7: SEM fractographs of the ordered Ni₃Fe with different stoichiometry when tested in H₂.

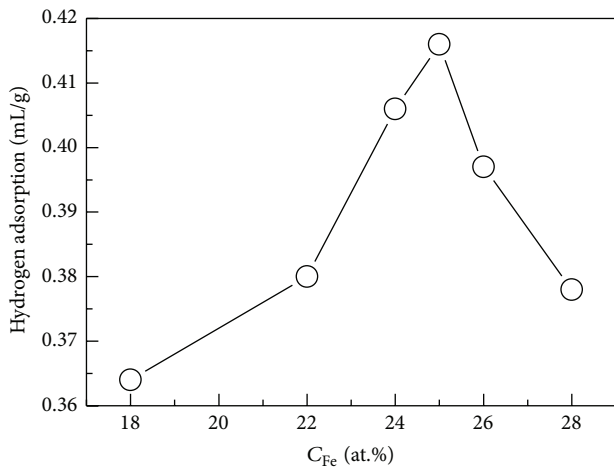


FIGURE 8: The curves of the quantity of hydrogen adsorption per gram for the ordered Ni₃Fe powder versus Fe stoichiometry.

stoichiometry. At the same precharging temperature, D_A of the ordered Ni₃Fe decreases with increasing Fe stoichiometry. The data of Table 2 demonstrate that Fe stoichiometry of the ordered Ni₃Fe alloy has a strong effect of reducing the hydrogen diffusion along the grain boundaries.

The relationship between the apparent hydrogen diffusion coefficient (D_A) of the ordered Ni₃Fe alloy with various Fe stoichiometries and reciprocal absolute temperature

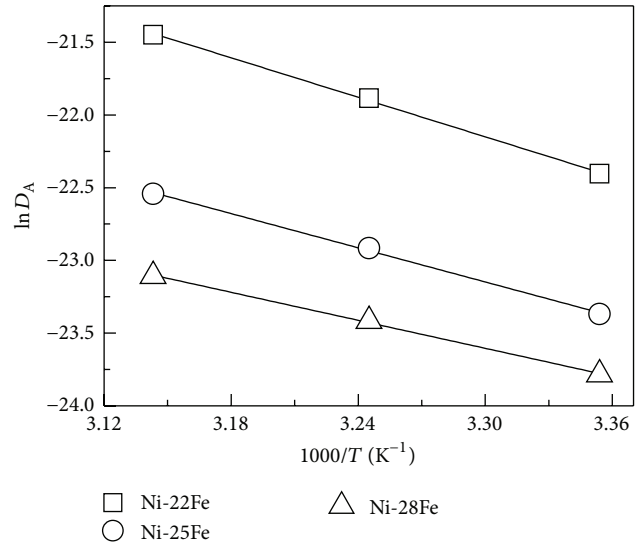


FIGURE 9: $\ln D_A$ versus $1/T$ for the ordered Ni₃Fe alloys with various stoichiometry.

is shown in Figure 9. There is a good linear relationship between $\ln D_A$ and T^{-1} for the ordered Ni₃Fe alloy. From Figure 9, the activation energy of hydrogen diffusion (Q) can be estimated for the ordered Ni₃Fe alloys and is also listed in Table 2. Figure 10 shows that there is a linear relation between the activation energy of hydrogen diffusion and Fe

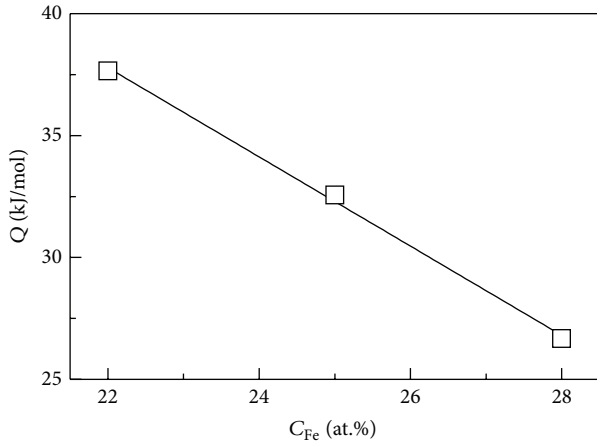


FIGURE 10: Relationship between the diffusion activation energy and Fe stoichiometry.

stoichiometry. Because the normal stoichiometric alloy has the highest degree of order in the ordered Ni_3Fe alloy, it can be deduced by the above experimental results that the diffusion coefficient and the activation energy of hydrogen diffusion are independent of degree of order of the alloy. This result means that the effect of Fe stoichiometry in the ordered Ni_3Fe alloy may influence grain-boundary chemistry which, in turn, affects hydrogen diffusion along the grain boundary.

Based on the above experimental results and discussions, we deduce that the effect of Fe stoichiometry on the susceptibility to hydrogen embrittlement is achieved by altering degree of order of the ordered Ni_3Fe alloy. The normal stoichiometric Ni_3Fe alloy has the highest degree of order; thus it has the highest ability of catalytic reaction and the highest susceptibility to hydrogen embrittlement. But Fe stoichiometry affects the behavior of hydrogen diffusion by influencing grain-boundary chemistry of the ordered Ni_3Fe alloy.

4. Conclusion

- (1) The mechanical properties and the susceptibility to hydrogen embrittlement of the ordered Ni_3Fe alloy vary with the Fe stoichiometry.
- (2) The normal stoichiometric Ni_3Fe alloy has the lowest mechanical properties, the highest susceptibility to hydrogen embrittlement, and the highest ability of catalytic reaction.
- (3) Degree of order is a key factor to influence susceptibility to hydrogen embrittlement of the ordered Ni_3Fe alloy.
- (4) The apparent hydrogen diffusion coefficient and the activation energy of hydrogen diffusion of the ordered Ni_3Fe alloy decrease with the increase of Fe stoichiometry.

Conflict of Interests

The authors declare that there is no conflict of interests regarding the publication of this paper.

Acknowledgments

This work was supported by the National Natural Science Foundation of China under Contract nos. 51271102 and 50671057. The authors also thank Instrumental Analysis and Research Center of Shanghai University for the help and support in the experiment and analysis of SEM.

References

- [1] T. L. Lin, "Recent advances in high-temperature ordered intermetallics," *Journal of Shanghai Jiaotong University*, vol. 32, no. 2, pp. 95–108, 1998.
- [2] P. Villars and L. D. Calvert, *Person's Handbook of Crystallographic Data for Intermetallic Phases*, vol. 3, ASM International, Materials Park, Ohio, USA, 1991.
- [3] I. Chichinas, V. Pop, and O. Isnard, "Magnetic properties of Ni_3Fe intermetallic compound obtained by mechanical alloying," *Journal of Magnetism and Magnetic Materials*, vol. 242–245, part 2, pp. 885–887, 2002.
- [4] G. M. Camus, N. S. Stoloff, and D. J. Duquette, "The effect of order on hydrogen embrittlement of Ni_3Fe ," *Acta Metallurgica*, vol. 37, no. 5, pp. 1497–1501, 1989.
- [5] Y. X. Chen, A. P. Chen, X. J. Wan, and S. R. Yan, "Ordering process and effect of ordering on the environmental embrittlement for Ni_3Fe alloy," in *The New Progress on Material Science and Engineering' 2004*, pp. 758–764, Chinese Materials Research Society, Metallurgical Industry Press, Beijing, China, 1st edition, 2004.
- [6] J. L. Wright and J. H. Zhu, "Environmental embrittlement of an ordered Ni-Mo alloy," *Scripta Materialia*, vol. 38, no. 2, pp. 253–257, 1997.
- [7] X. J. Wan, Y. X. Chen, A. P. Chen, and S. R. Yan, "The influence of atomic order on H_2 -induced environmental embrittlement of Ni_3Fe intermetallics," *Intermetallics*, vol. 13, no. 5, pp. 454–459, 2005.
- [8] Y. Liu, C. T. Liu, L. Heatherly, and E. P. George, "Effect of boron on the fracture behavior and grain boundary chemistry of Ni_3Fe ," *Scripta Materialia*, vol. 64, no. 3, pp. 303–306, 2011.
- [9] C. T. Liu, C. L. White, and J. A. Horton, "Effect of boron on grain-boundaries in Ni_3Al ," *Acta Metallurgica*, vol. 33, no. 2, pp. 213–229, 1985.
- [10] Y. Chen, H. Y. Qian, and T. Chen, "The effect of stoichiometry and degree of order on mechanical properties of Ni_3Fe intermetallics," *Materials Science Forum*, vol. 747–748, pp. 19–24, 2013.
- [11] Y. X. Chen, J. Ma, and C. T. Liu, "Hydrogen diffusivity in B-doped and B-free ordered Ni_3Fe alloys," *Intermetallics*, vol. 19, no. 1, pp. 105–108, 2011.